The anelasticity of zinc and its implications for the Earth's inner-core

Simon A Hunt[1], Andrew M. Walker[2], Oliver T Lord[3], Stephen Stackhouse[4], Lewis Schardong[5], Lora S Armstrong[6], Andrew J Parsons[7], Geoffrey LLoyd[8], John Wheeler[9], and Matthew L. Whitaker[10]

[1]University of Manchester
[2]Department of Earth Sciences, University of Oxford,
[3]University of Brstol
[4]University of Leeds
[5]Raymond & Beverly Sackler Faculty of Exact Science
[6]Delft University of Technology
[7]University of Oxford
[8]University of Leeds, UK
[9]University of Liverpool
[10]Mineral Physics Institute, Stony Brook University

November 22, 2022

Abstract

Seismic observations of the Earth's inner-core testify to it being both a complex and dynamic part of the Earth. It exhibits significant variation in seismic attenuation and velocity with position, depth and direction. Interpretation of which is difficult without knowledge of the anelastic processes active in the inner-core is difficult. To address this, we used zinc, a low-pressure analogue of the hexagonal close pack (*hcp*) structured iron that forms the inner-core, to provide first-order constraints on the anelasticity of *hcp*-metals at high pressure, seismic frequencies (0.003-0.1Hz), homologous temperatures (T/T_m) up to 0.8. Measurements were made in a deformation-DIA combined with X-radiography. The data was analysed using an improved image processing method that reduces systematic errors and improves strain measurement precision by up to 3 orders of magnitude. Using this algorithm significant dissipation and softening of zinc's Young's modulus is observed. The softening occurs in the absence of significant impurities or a fluid phase and is caused by grain boundary sliding coupled with dynamic recrystallisation.The recrystallisation results in a steady-state grain-size and low dislocation density. A softened Young's modulus predicts a reduction in shear wave speed 2-3 times greater than that for compressional waves, which is consistent with anelasticity playing a significant role in the seismic velocity of the inner-core. Comparison of elastic wave speeds from experimental or computed material properties with anelastically-retarded inner-core seismic velocities will tend to over-estimate the light element budget of the inner-core. Therefore anelastic effects in *hcp*-iron must be considered in the interpretation of the inner-core.

The anelasticity of zinc and its implications for the Earth's inner-core

Simon A. Hunt[1,2], Andrew M. Walker[3,4], Oliver T. Lord[5], Stephen Stackhouse[3], Lewis Schardong[2,6], Lora S. Armstrong[7], Andrew J. Parsons[3,4], Geoffrey E. Lloyd[3], John Wheeler[8], Matthew L. Whitaker[9]

[1]Department of Materials, University of Manchester, Oxford Rd, Manchester M13 9PL, UK
[2]formerly at: Department of Earth Sciences, University College London, Gower Street, London. WB1E 6BS. UK
[3]School of Earth and Environment, University of Leeds, Leeds LS2 9JT, UK
[4]now at: Department of Earth Sciences, University of Oxford, South Parks Road, Oxford, OX1 3AN, UK
[5]School of Earth Sciences, University of Bristol, Wills Memorial Building, Queen's Road, Bristol BS8 1RJ, UK
[6]Dept. of Geosciences, Raymond & Beverly Sackler Faculty of Exact Sciences, Tel Aviv University, Israel
[7]Department of Geoscience and Engineering, Delft University of Technology, 2628 CN Delft, The Netherlands
[8]School of Environmental Sciences, Jane Herdman Laboratories, University of Liverpool, Liverpool, UK
[9]Mineral Physics Institute, Department of Geosciences, Stony Brook University, Stony Brook, NY 11794-2100 USA

Key Points:

- The inner-core analogue zinc shows anelastic softening at seismic frequencies and high temperatures
- Substantial anelastic softening is possible even in the absence of a fluid or significant impurities
- Anelasticity should be accounted for when interpreting the inner-core's seismic velocity and structure

Corresponding author: Simon A. Hunt, `simon.hunt@manchester.ac.uk`

Abstract

Seismic observations of the Earth's inner-core testify to it being both a complex and dynamic part of the Earth. It exhibits significant variation in seismic attenuation and velocity with position, depth and direction. Interpretation of which is difficult without knowledge of the anelastic processes active in the inner-core is difficult. To address this, we used zinc, a low-pressure analogue of the hexagonal close pack (*hcp*) structured iron that forms the inner-core, to provide first-order constraints on the anelasticity of *hcp*-metals at high pressure, seismic frequencies (~0.003–0.1 Hz), homologous temperatures (T/T_m) up to $\approx$ 0.8. Measurements were made in a deformation-DIA combined with X-radiography. The data was analysed using an improved image processing method that reduces systematic errors and improves strain measurement precision by up to 3 orders of magnitude. Using this algorithm significant dissipation and softening of zinc's Young's modulus is observed. The softening occurs in the absence of significant impurities or a fluid phase and is caused by grain boundary sliding coupled with dynamic recrystallisation. The recrystallisation results in a steady-state grain-size and low dislocation density. A softened Young's modulus predicts a reduction in shear wave speed 2-3 times greater than that for compressional waves, which is consistent with anelasticity playing a significant role in the seismic velocity of the inner-core. Comparison of elastic wave speeds from experimental or computed material properties with anelastically-retarded inner-core seismic velocities will tend to over-estimate the light element budget of the inner-core. Therefore anelastic effects in *hcp*-iron must be considered in the interpretation of the inner-core.

1 Introduction

The solid inner-core is the most remote and inaccessible part of our planet but its structure and composition may provide constraints on the geological history of the surface environment. Information encoded in the inner-core during its solidification could reveal the timing and nature of the onset of Earth's protective magnetic field generated by convection in the liquid outer core or even of changes in the way the mantle convects and drives surface dynamics [e.g. *Aubert et al.*, 2008]. Key to developing our understanding of the inner-core is our ability to use seismic observations to constrain its structure on all scales. Both seismic velocities recovered from body wave studies (typical frequency 0.5 - 1.5 Hz) and normal modes (frequency <10 mHz) are strongly sensitive to the atomic-scale crystal structure, temperature and composition of the media through which they travel. They are also sensitive

to the larger grain-scale microstructure, which reflects the deformation and crystallization history of the medium and can be probed by seismic studies of elastic anisotropy (variation of wave velocity with direction), dispersion (variation of wave velocity with frequency) and attenuation (reduction in wave amplitude with distance). However, the experimental data needed to link inner-core seismic observations to microscopic physical behaviour is lacking.

It is widely accepted that iron in the inner-core adopts the hexagonal close packed (*hcp*) structure stable above 10 GPa [e.g. *Tateno et al.*, 2010], albeit diluted by a light element [*Bazhanova et al.*, 2017; *Fei et al.*, 2016; *Antonangeli et al.*, 2018, 2010; *Fiquet*, 2001; *Mao et al.*, 2012; *Caracas*, 2015; *Sakamaki et al.*, 2016; *Tagawa et al.*, 2016; *Tateno et al.*, 2012, 2015; *Prescher et al.*, 2015; *Li et al.*, 2018]. However, *Belonoshko et al.* [2019] argued that anelasticity of the inner-core is incompatible with that observed for *hcp* metals, and instead suggested that iron adopts a body centred cubic (*bcc*) structure in the inner-core. In general, experimental and computational studies investigating inner-core properties and chemistry, implicitly assume negligible anelastic attenuation and no modification to the seismic wave speed.

The anisotropy of the inner-core is well established [*Sumita and Bergman*, 2015; *Deuss*, 2014; *Woodhouse et al.*, 1986] with higher velocities in the polar direction than the equatorial plane [e.g. *Morelli et al.*, 1986]. The top 50-275 kms of the inner-core are isotropic [*Shearer*, 1994; *Irving and Deuss*, 2011] but there are differences between the Eastern and Western hemispheres [*Niu and Wen*, 2001] and seismic velocity anisotropy increases with depth into the inner-core [*Lythgoe et al.*, 2014].

Along with seismic velocity, seismic attenuation, Q^{-1}, is a direct measurement of inner-core properties and is the inverse of the seismic quality factor. The seismic quality factor, Q, is equal to the fraction of energy absorbed per oscillation of a wave [*Stein and Wysession*, 2013; *Romanowicz and Mitchell*, 2015]. An undamped oscillator with no attenuation or energy loss has $Q = \infty$ ($Q^{-1} = 0$). Using body waves, Q has been estimated for the inner-core to be ~200 just below the inner-core boundary increasing to 1000–2000 at the center of the Earth [*Doornbos*, 1974]. Significant regional variation in Q has been found to exist by *Pejić et al.* [2019] and *Li and Cormier* [2002], with a global mean $Q_{1\,\mathrm{Hz}} \sim 300$. Attenuation is also anisotropic [e.g. *Yu and Wen*, 2006], with hemispherical [*Cao and Romanowicz*, 2004] and depth variations [*Suda and Fukao*, 1990] observed. Using normal modes, *Mäkinen et al.* [2014] showed that attenuation in the inner-core is directionally dependent with the

North-South direction being both seismically faster and more attenuating than radial directions.

Microscopically, attenuation is caused by mechanically reversible and thermodynamically irreversible strain accommodation mechanisms [*Li and Wagoner*, 2021]. These are any mechanism by which strain can be accommodated, for example the flow of trapped fluids [e.g. *Singh*, 2000; *Fearn et al.*, 1981], phase transitions [*Li and Weidner*, 2008] or the iron spin-transition [*Marquardt et al.*, 2018]. Within solid phases strain is accommodated by the classic deformation mechanisms e.g. diffusion creep, dislocation motion, grain boundary sliding and twinning. The characteristic behaviours of all of these mechanisms are dependent on the time-scale (frequency or duration) and stress magnitude as well as the temperature, pressure and microstructure. The time dependent nature of the dissipation leads to frequency-dependent moduli and seismic velocities.

Attenuation mechanisms that have been proposed for the inner-core include partial melt [*Singh*, 2000; *Fearn et al.*, 1981], grain boundary relaxation, and dislocation related relaxations [*Jackson et al.*, 2000]. *Mäkinen et al.* [2014] preferred Zenner relaxation to explain inner-core attenuation; in this mechanism Fe atoms switch positions with vacancies and/or solute atoms as a result of the stress imparted by the passing seismic wave. All of these have been observed in geological samples or metals, albeit at less extreme conditions than those of the inner-core.

The experimental data needed to distinguish between the proposed atttenuation mechanisms in seismological observations does not exist because of the extreme conditions under which *hcp*-iron is stable. There are no measurements of anelasticity in *hcp* metals at significant pressure and temperature. The most recent study of the anelasticity of iron [*Jackson et al.*, 2000] is over two decades old and is limited to low pressures where iron adopts the body centred cubic (*bcc*) or face centred cubic (*fcc*) structure.

Low-pressure analogues are commonly used when deep Earth conditions are too extreme to be accessible experimentally, leading to various *hcp* metals including zinc, titanium, magnesium and cobalt being utilised as analogues for the inner-core. Anelasticity experiments have been performed on *hcp* metals at ambient pressure but are generally at much higher frequencies than seismic waves [e.g. *Wuttig et al.*, 1981; *Aning et al.*, 1982; *Takahashi*, 1952], or inferred from large strain creep tests [e.g. *Li and Wagoner*, 2021]. One rare example of a seismic frequency investigation is that of *Roberts and Brown* [1962], who mea-

sured the anelasticity of *hcp* zinc with periods between 10 and 100 seconds and attributed the anelasticity to dislocation motion.

In using analogues, some consideration must be taken for the differences in conditions and chemical behaviour between the analogue and Earth forming phase. The ideal c/a axial length ratio in the *hcp* structure is 1.63 and is 1.50-1.62 in *hcp*-iron [*Fischer and Campbell*, 2015]. The c/a ratio is 1.62 in Mg and 1.88 in Cd. In zinc it is 1.87 at ambient pressure and decreases with pressure, reaching the ideal c/a ratio of 1.633 at ~30 GPa [*Kanitpanyacharoen et al.*, 2012]. The slip system activities and deformation fabrics depend on the c/a ratio of the unit cell [*Wang and Huang*, 2003], although *Poirier and Price* [1999] argued that stacking fault energy is a better predictor of slip systems than c/a ratio. Twinning is also a significant deformation mechanism in *hcp* metals [e.g. *Price*, 1961; *Kanitpanyacharoen et al.*, 2012; *Liu et al.*, 2020]. Despite the differences in slip systems, deformation mechanism maps are consistent between *hcp* metals after scaling for the elastic shear modulus and homologous temperature (T/T_M, where T is the temperature and T_M is the melting temperature) [e.g. *Frost and Ashby*, 1982]. For example, both zinc and *hcp*-iron undergo dynamic recrystallisation significantly below their melting temperatures [*Frost and Ashby*, 1982; *Anzellini et al.*, 2013] and deform by both basal and prismatic slip on equivalent slip systems [*Miyagi et al.*, 2008; *Merkel et al.*, 2004; *Yoo and Wei*, 1967; *Yoo et al.*, 2001].

The inner-core is close to its melting temperature but there are no reported *hcp*-iron deformation experiments at those conditions; the highest temperature that *hcp*-iron has been deformed at is 1000 K (and 30 GPa, $T/T_M \sim 0.4$) [*Merkel et al.*, 2004]. However, other *hcp* metals have been deformed close to their melting temperatures. For example, *Bergman et al.* [2018] deformed columnar and untextured zinc-tin alloy close to its melting temperature ($T/T_M = 0.97$) and reported that columnar samples deformed by grain boundary sliding and untextured samples, with a smaller grain-size, by diffusion creep at the same strain-rates.

The similarity of deformation mechanism between *hcp* metals [*Yoo and Wei*, 1967] indicates that the crystal structure plays a fundamental role in deformation mechanisms. Anelastic dissipation occurs via processes controlled by crystallography (e.g. dislocations, diffusion) and it is therefore reasonable to assume a first-order similarity exists between anelastic deformation mechanisms too.

To address the lack of anelasticity data at seismic frequencies in *hcp* metals, we measured the anelastic response of zinc at high pressure and homologous temperatures up to 0.8.

The remaining sections of this paper describe the experimental method, an improved approach to data processing needed to extract the anelastic response, the derivation of a model of anelasticity that fits our results, and a discussion of the significant softening observed in the measurements and the implications of this for our understanding of the inner-core.

2 Experimental Method

This study utilises the experimental method of *Li and Weidner* [2007] to measure the anelastic response of zinc relative to an elastic reference. Small-amplitude sinusoidal strains were applied to an experimental column consisting of a zinc sample and corundum elastic standard, whilst simultaneously acquiring X-radiographic images. Uniaxial strains in the sample and standard were determined by tracking displacement of marker foils in the X-radiographs with an improved image processing algorithm. Strain in the elastic standard is used as a proxy for stress, which combined with the sample strain and phase lag of the sample relative to that of the elastic standard, is sufficient to determine the anelastic response of the sample. Additional samples were cold-compressed or annealed at high pressure to show how the microstructure and crystallographic fabric is affected by the sinusoidal deformation.

2.1 Samples

Two different samples were used in this study. A sample of 1 mm diameter high-purity zinc wire (99.9985 % metal basis, Puratronic from Alfa Aesar) and a sample of fine-grained zinc powder (99% metal basis, 75 µm particle size, that had not been stored in an inert atmosphere) from Sigma Aldrich; hereafter referred to as *'wire'* and *'powder'* samples respectively. High-resolution X-ray diffraction of the zinc powder shows it to contain trace amounts of two forms of ZnO (cubic and hexagonal) and at least one form of $Zn(OH)_2$. The wire samples were prepared by polishing to ~1–1.3 mm lengths and the powder samples were pressed into similarly long, 1 mm diameter pellets in a steel die with flat-ended pins. For the compression and annealing experiments, the powder sample was wrapped in 25 µm gold foil, to ensure it could be distinguished from the wire when recovered.

The elastic standards were 1 mm diameter solid rods of Alsint-23 corundum, from Alfa Aesar. Each piece was polished to <0.9 mm long with flat parallel ends. Two pieces were used on either end of the zinc samples in the anelasticity experiments to keep the cell symmetrical and to guarantee that at least one standard could be observed in the X-radiographs.

Disks of 25 μm thick platinum foil were used as markers between the samples and corundum standards as well as at the outer ends of the corundum standards. Corundum pistons were also used in the compression and annealing experiments to keep the sample environments consistent.

2.2 Anelasticity experiments

The anelasticity experiments were performed in the D-DIA [*Durham et al.*, 2002; *Wang et al.*, 2003] on beam-line X17B2 at the NSLS, Brookhaven National Laboratory, New York.

The sample assembly for the experiments consisted of a 6.1 mm cube of pyrophyllite baked to 1000°C. A 3.0 mm diameter hole drilled through the pyrophyllite contained a crushable alumina sleeve, 2.36 mm outer, 2.10 mm inner diameter graphite furnace and a 1.8 mm outer diameter, 1.0 mm inner diameter, 3.0 mm long boron nitride sleeve. The sample stack was inserted into this boron nitride sleeve and capped at the ends by crushable alumina. A C-type thermocouple inside a 0.8 mm diameter 4-bore alumina rod was inserted radially with its hot junction just inside the furnace and did not touch the sample. A cross-section of the cell assembly used here is included in *Dobson et al.* [2012a].

Before each experiment was compressed, the 10-element energy dispersive X-ray diffraction detector [*Weidner et al.*, 2010] was calibrated using a corundum standard, with 10 minute exposure, and open-press measurements were taken from both the zinc and corundum samples, with 5 minute exposures. Each experiment was compressed to the desired end-load over ~2 hours. After heating to the desired temperature, further diffraction patterns were acquired from both sample and standard. The zinc diffraction volume was in the centre of the sample and that of the corundum in the part closest to the zinc. The samples were then strained sinusoidally at periods of 10, 30, 100 and 300 s by driving the D-DIA's deformation pumps. During sinusoidal deformation, the total load on the system was kept constant by retracting or advancing the main ram in response to changes in the force applied by the differential pumps. This minimises any changes in pressure applied to the sample. It was not possible to acquire shorter period data due to the mechanical limits of the D-DIA system and time constraints prevented the acquisition of data with longer periods. The amplitude of the deformation was the minimum needed to observe sinusoidal strains in both the sample and elastic standard using the software available when the experiments were performed (see sec-

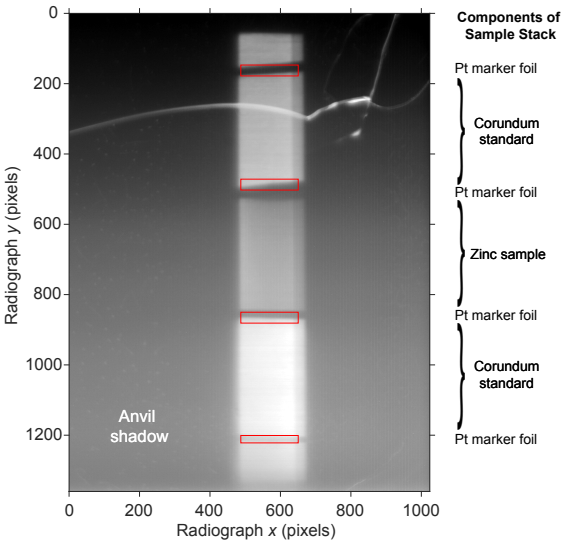

Figure 1. Example X-radiograph from Zinc powder experiment Zn_08 at 240 kN, 117 °C and 100 s period. The bright stripe in the center of the image contains the sample and corundum standards, as annotated on the right hand side. The red boxes are the positions of the regions of interest tracked between images. The dark areas at either side of the image are the shadows of the tungsten carbide anvils and the bright curved cross-cutting feature in the top third of the image is a crack in the YAG scintillator. The scale of the image is 2 µm/pixel.

tion 3.1). During each deformation experiment, X-radiographs were acquired using a yttrium aluminium garnet scintillator and a visible-light camera, for a minimum of 10 nominal periods. Between 20 and 40 X-radiographs were collected per driving period, with an exposure time of 0.3 s. A typical radiograph is shown in Figure 1. After all data had been acquired at each temperature, the temperature was changed and the cycle repeated. In some experiments the pressure was then increased and the data acquisition cycle repeated. Data was acquired during both increasing and decreasing temperature steps, to confirm that the results are not affected by the thermal history of the sample. The maximum temperature at which the data reported here was collected was 400 °C (a homologous temperature of ~0.8). Processing of the X-radiographs is discussed in section 3.

A further D-DIA experiment was performed to confirm there are no significant temperature differences between the thermocouple, sample and corundum standard. This experiment used the melting curve of zinc [*Errandonea*, 2010] as an independent constraint and the measured pressure and temperature were within error of the melting curve when the zinc sample melted. Full details of the experiment are included in Appendix A.

2.3 Compression and annealing experiments

Powder and wire samples were enclosed in an octahedral assembly for compression in a Walker-type multi-anvil [*Walker et al.*, 1990] at University College London. The sample assembly consisted of a 18 mm edge length chrome-doped MgO octahedron, that was compressed by anvils with 10 mm corner truncations. The samples and corundum pistons were contained in a boron nitride sleeve and heating was via a straight graphite furnace (4.1 mm outer diameter, 3.5 mm inner diameter). A thermocouple was inserted through the furnace with the hot junction positioned between the two samples.

The experiments were compressed to ~ 4 GPa over 2 hours. The compression experiment was then decompressed over 3 hours. The annealing experiment was heated to 300 °C for 4 hours before slow decompression. The samples from these experiments are referred to as *'compressed'* and *'annealed'* samples respectively.

2.4 Diffraction pattern analysis

The pressure in the anelasticity experiments was calculated from the energy dispersive corundum diffraction patterns. Although zinc is more compressible and should give more precise pressure estimates, above ~200°C its diffraction patterns ceased to reliably contain the multiple diffraction peaks needed to determine volume strains. Individual peaks would rapidly increase and decrease in relative intensity, as the zinc underwent rapid recrystallisation.

At each pressure–temperature condition there are 10 independent diffraction patterns, corresponding to each element of the detector. The distinguishable diffraction peaks were fitted in each pattern using the software package 'Plot85' and fit to determine the unit cell volume. Volume strains were calculated independently for each of the detector elements using the corresponding open-press unit cell volume, the corundum thermal expansion coefficients of *Fei* [1995] and the temperature reported by the thermocouple. There was no significant temperature offset between the corundum and thermocouple as confirmed using the melting curve as an independent constraint (see Appendix A).

Pressures were calculated, independently for each detector, from the volume strain, assuming a bulk modulus of $K_0 = 254.28$ GPa along with pressure and temperature derivatives of $K' = 4.27$ and $\mathrm{d}K/\mathrm{d}T = -0.0173\,\mathrm{GPa\,K^{-1}}$ respectively. The bulk modulus and the

temperature derivative are a linear fit to the Voigt-Reuss-Hill bulk moduli calculated using MSAT [the Matlab Seismic Anisotropy Toolbox, *Walker and Wookey*, 2012] from the elastic stiffnesses (c_{ij}s) of *Goto et al.* [1989]. The pressure derivative was calculated from the pressure dependencies of the elastic stiffnesses of *Gieske and Barsch* [1968] in the same manner, assuming the derivatives are linear at pressures greater than 1 GPa. The pressures reported in Tables 1 and 2 are the weighted mean and standard deviation of the values calculated from all the detector elements. Elastic stiffnesses were used, rather than an Equation of State, for internal consistency with subsequent calculations of Young's modulus (Section 4).

2.5 Electron Microscopy analysis

All experimental samples were mounted in epoxy resin and polished for analysis in the FEI Quanta 650 field emission gun (FEG) scanning electron microscope at the University of Leeds. Prior to mounting, the compressed and annealed samples were removed from the pressure medium but the anelasticity samples were not. The final finish was a 0.03 µm colloidal silica chemo-mechanical polish in an alkaline solution [*Lloyd*, 1987]. Electron Back-Scatter Diffraction (EBSD) measurements were obtained using a 20 kV accelerating voltage, a spot size of 65 µm and a working distance of 27 mm. The step size was ~1 µm. The Kikuchi patterns were automatically indexed using Oxford Instrument's AZtec software package. Zinc metal, ZnO, two forms of $Zn(OH)_2$ and Al_2O_3 were listed as possible phases during indexing.

Analysis of the EBSD data were performed using MTEX v5.5.1 [*Bachmann et al.*, 2010, 2011] and CrystalScape v2.0.2, a software package for analysing EBSD data which includes a method for relating intracrystalline distortion to dislocation density [*Wheeler et al.*, 2009]. Grains were reconstructed in MTEX with the threshold misorientation-angle that indicates a grain boundary, set at 10°. Some of the samples retained significant surface scratching which influences the grain reconstruction. To account for this, data from grains that were within the surface scratches were discarded and the grain-reconstruction rerun. The twin plane was identified from the annealed wire sample by finding the most common grain-grain misorientation relationships. Twin boundaries were identified in the samples and grains merged if the misorentation between adjacent grains was within 5° of the twin plane.

Grain-grain misorientation distributions were calculated using CrystalScape and the method of *Wheeler et al.* [2001]. Neighbour-pair misorientation angles were calculated for

adjacent pixels that are separated by grain-boundaries as defined by the 10° grain boundary misorientation threshold. Random-pair distributions were also calculated for misorientations between 10 and 80°. The upper threshold was utilised to remove the effect of twinning on the distributions, which are not accounted for by CrystalScape. Significant differences between these two distributions are indicative that neighbouring grains have some common inheritance or interaction [*Wheeler et al.*, 2001] but statistical tests were not performed on the misorientation angle distributions because the distributions are weighted here by the length of each grain boundary segment, significantly skewing any probabilities.

The Weighted Burgers Vector is calculated as a proxy for dislocation density in the samples. The Weighted Burgers Vector is calculated from the local curvature of the crystal lattice, quantified using gradients in crystal orientation [*Wheeler et al.*, 2009] and has units of $(\text{length})^{-1}$; units of μm^{-1} prove convenient. High angle boundaries will not have an organised geometrically necessary dislocation structure and should be excluded from gradient calculations. We err on the side of caution here and exclude from calculations any misorientation of more than 5 degrees between pixels. The magnitude of the vector is strongly correlated with other measures of lattice distortion [e.g. Kernal Average Misorientation, *Hielscher et al.*, 2019]. With additional assumptions about slip systems, dislocation densities can be calculated. These are not necessary here as our aim is to *compare* datasets from a particular material.

Similarly, converting the grain-size inferred from the EBSD reconstruction into a three-dimensional grain volume requires making assumptions about the grain shape in three dimensions, about which we have no information. In the analysis here we are only concerned with comparative grain-size between samples and therefore no attempt to determine three-dimensional grain volumes has been made.

3 X-Radiograph Analysis

In order to determine the anelasticity of the zinc samples, we need to track the amplitude and phase of strain in the zinc and corundum (used as a proxy for stress) during the experiment. To do so with sufficient precision, we had to develop an improved analysis method for processing the sequences of X-radiographs collected during sinusoidal deformation.

3.1 Prior work

The algorithm used here, for sub-pixel tracking of marker foil displacements in X-radiographs, is based on the image processing algorithms of *Pratt* [1991] and *Trucco and Verri* [1998] and was initially implemented for X-radiographs by *Li et al.* [2003]. The basis of the algorithm is finding the minimum of the Sum Squared Differences (SSD) in pixel intensity between regions of interest in a reference image ($I_r\{X,Y\}^b$) and a search region in the comparison image (I_c) where $\{X,Y\}^b$ is the array of pixel coordinates for region of interest b. The SSD of the pixel intensities between the two images is calculated for a range of offsets, o, as:

$$D^b_{r,c}(o) = \sum_i \sum_j \left[I_r\{X,Y\}^b - I_c\{X,Y+o\}^b \right]^2 \tag{1}$$

An example set of $D^b_{r,c}(o)$ are plotted as black crosses in Figure 2a. The displacement ($d^b_{r,c}$) of the region of interest, and hence the marker foil, is found with subpixel resolution by finding the minimum of a cubic spline interpolated between the values of $D^b_{r,c}(o)$. The offset range, o, used to determine the displacement, is generally ±5 pixels (10 µm) vertically in the image (y-direction in Figure 1). *Li et al.* [2003] were primarily interested in tracking comparatively large total displacements (0-10 pixels) during deformation experiments and tracked the displacement between consecutive pairs of images ($d_{r=1,c=2}$, $d_{r=2,c=3}$, ... $d_{r=N-1,c=N}$, where N is the total number of images) . In this framework, the position of the region of interest changes as the marker foil moves and the total displacement of each region of interest is the sum over all prior displacements. The position of the marker foil in image n:

$$P^b(n) = P^b_0 + \sum_{r=1}^{n} d^b \tag{2}$$

where P_0 is the initial position of the region of interest determined from the mean pixel Y values in that region.

The sample length, l, at each time step is the difference in position of two regions of interest above and below the sample:

$$l(n) = P^{b+1}(n) - P^b(n) \tag{3}$$

Time stamps of each image are used to convert the length as a function of frame number, n, into length as a function of time, t.

This algorithm has been utilised most often to measure strain in high-strain deformation experiments [e.g. *Li et al.*, 2003; *Dobson et al.*, 2012b; *Hunt et al.*, 2019, 2010]. *Dobson*

et al. [2008, 2010] used this algorithm to measure small sinusoidally varying displacements during thermal conductivity experiments. *Hunt et al.* [2011, 2012] improved the precision in similar thermal conductivity experiments by using the central radiograph in 100–1000 image long time series as a single reference ($d_{r=N/2,c=1}$, $d_{r=N/2,c=2}$, ... $d_{r=N/2,c=N}$) and utilising a degree-6 polynomial rather than a spline to find the minimum of the SSD. These studies were primarily interested in the phase differences and not specifically concerned with the amplitude of the sinusoidal displacements. In this study, good constraints on both the amplitude and phase of the strain are critical. Both the original and improved algorithms returned signals that were too variable for the reliable extraction of anelastic properties. We have therefore further refined the algorithm to return more consistent and precise displacements of the marker foils.

3.2 Refined algorithm

To gain precision in the image processing, rather than treating each pair of images in isolation and then interrogating the displacements, we describe all the SSD for a sequence of images, $D(o,t)$, as a single polynomial surface, $S(o,t)$ (Figure 2a). The surface has degree m in offset (o), n in time (t) and the total degree of the polynomial surface is the greater of m and n [*Gallier*, 2000]. For $m > n$, the surface is:

$$S^b(o,t) = \sum_{u=0}^{m} \sum_{v=0}^{\min(n,m-u)} C_{uv}\, O(t)^u\, t^v, \tag{4a}$$

where C_{uv} are the polynomial coefficients and O is a modified form of the pixel offset (o) that accounts for the sinusoidal displacement of the foils:

$$O(t) = o + a\sin(ft + \phi), \tag{4b}$$

where a is the amplitude, ϕ the phase and f the frequency of the displacement. If the amplitude, a, of the sinusoidal displacement is zero then $O = o$ and Equation 4 is no longer a function of time.

The surface $S(o,t)$ is fit to $D(o,t)$ by ordinary least-squares minimisation. The fit is performed simultaneously for all the regions of interest with independent surface coefficients for each region of interest and the period of the driving force as the only common parameter. For these experiments, with sequences longer than 200 images, $m = 6$ and $n = 3$ were found to be sufficient to reproduce the shape of the SSD surface and capture the displacement's phase and amplitude. It was found that lower-degree surfaces do not fully capture the shape

of the $D(o,t)$ surface while higher-degree surfaces have artefacts in the fit. The formal errors in the period, phase and amplitude in the surface fit are typically 0.002 s, 0.01 radians and 0.001 pixels respectively and, for the 300 s data, up to 3 orders of magnitude smaller than those for the previous fitting method (Section 3.1).

Figure 2a shows the $D(o,t)$ values from the first (top) region of interest from the zinc powder experiment at ~117 °C and 100 s period. This clearly shows the significant increase in $D(o,t)$ with offset as the intensity mismatch between the regions of interest in the reference and comparison images get larger. The sinusoidal displacements of the marker foil with time is reflected in the sinusoidal variation of D with time at constant offset. The fitted surface, $S(o,t)$, is shown in Figure 2b and is a good description of the data. The residuals of the fit (Figure 2c) are small and not systematic with time.

The least-squares residuals form a bow-tie shape in offset (Figure 2c). This is because at small offsets the intensity differences are small and the addition of noise to small differences squared has less effect than at large offsets where the intensity differences increase. For example, the addition of 1 arbitrary unit of noise to an intensity difference of 3 increases the difference squared from 9 to 16 (difference of 7) whereas 1 arbitrary unit to an intensity difference of 10 increases the difference squared from 100 to 121 (difference of 21).

The displacement of each region of interest, $d^b(t)$, is the minimum of the surface with respect to time:

$$d^b(t) = \arg\min S^b(t), \tag{5}$$

which is found by differentiation of the polynomial surface, $S^b(o,t)$, with respect to offset. This minimum is sinusoidal in time, retaining the sinusoidal component of O (Equation 4b). Because the reference image is now a single image, the position of the marker foil is now:

$$P^b(t) = P^b_r + d^b(t), \tag{6}$$

rather than the sum it was previously (Equation 2). The sample length can be calculated as previously (Equation 3) but because $P^b(t)$ is an algebraic expression, length is instead calculated by combining the polynomial and sinusoidal components of the displacements algebraically, to give both a secular length change over the experiment and a single sinusoidal amplitude (A) and phase angle (Φ). This sum has to account for the phase of the sinusoidal displacement at the time of the reference image; if the reference coincided with either extrema of the sinusoidal wave, a small error would be added to the length of the samples and propagated into the subsequent calculations.

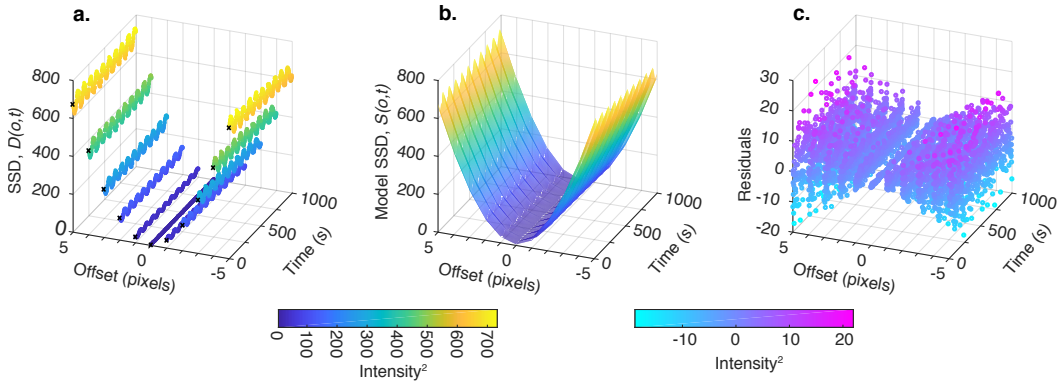

Figure 2. Example of Sum Squared Differences (SSD) data and its fit with our improved algorithm. (a) SSD data, $D(o,t)$, for the first (top) region of interest plotted against time from Zinc powder experiment Zn_08, at ~117°C with 100 s period. The first set of values, at $t = 0$, are highlighted by black crosses. The reference image is shown in Figure 1. (b) The best fit surface, $S(o,t)$, to the data and (c) the residuals $(D(o,t) - S(o,t))$. The values of $D(o,t)$ and $S(o,t)$ are in arbitrary units squared. The marker foil displacement is the minimum of the SSD at each time step (Equation 5). The sinusoidal displacement (here <0.1 pixels) is reflected in the sinusoidal variation in SSD values at constant offset. The combination of displacements above and below a region gives the length changes which are plotted in Figure 3.

The largest source of error, in this calculation, is the absolute length of the sample, which *Li et al.* [2003] argued to be ±5 pixels. To minimise both the absolute and relative length error between data acquisitions, the regions of interest were positioned automatically . Horizontally, the regions of interest were centred in the bright part of the image and ended close to but not overlapping with the anvil shadows. The regions of interest not adjacent to the zinc sample (Figure 1, top and bottom red boxes) were centred over the minimum in a spline interpolation of the intensity profile; the width and depth remained very similar throughout the experiment. The regions of interest adjacent to the zinc sample became broader throughout the experiment as the platinum marker foil diffused into the zinc. To account for this, the regions of interest were centred over the maximum gradient (as interpolated by a spline) on the side of the foil away from the sample. The sample lengths were subsequently adjusted to account for the thickness of the platinum foil; half a foil thickness, 12.5 µm or 7 pixels, was subtracted from the lengths of the corundum standards and 25 µm (14 pixels) from the zinc sample length.

Figure 3 shows the length change and our fits for the corundum standard and zinc sample as a function of time, for the same data set illustrated in Figures 1 and 2. The secular

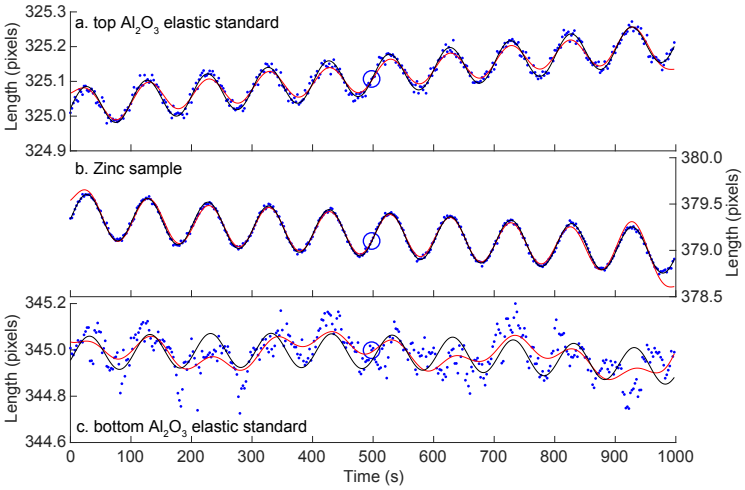

Figure 3. Elastic standard (a, c) and zinc sample lengths (b) calculated by the SSD image analysis for the same data shown in Figures 1 and 2. Blue dots are minima of the SSD polynomial for independent calculations of the displacement between each radiograph and the standard and the red lines are the fit to the minima calculated using the method of *Hunt et al.* [2011, 2012]. The black lines are the length changes calculated from the surface fits to all the SSD data (Figure 2) and thus not not fits to the points, but ideally they should reproduce them. The large blue circles highlight the length in the reference image. The anelastic dissipation was calculated using only the strains from the top corundum standard.

length change for the new algorithm is formally a degree-3 polynomial, because $n = 3$, but appears to be approximately a degree-1 polynomial because the higher order terms are small. For the zinc sample (Figure 3b), which had a relatively large deformation amplitude, both the method used previously by *Hunt et al.* [2011, 2012] (red lines) and the new method (black lines) are good fits to the length change values and give virtually the same values for A, f and Φ. The biggest differences between the values and the fits is at the beginning and end of the time series and arises from how the secular length change is dealt with by the previous methods' fit [see *Hunt et al.*, 2011, 2012, for details].

For the smaller-amplitude corundum values (Figure 3a, c) the algorithmic improvements in the fit are more significant with the new algorithm overcoming the systematic underestimation of amplitude present in the previous algorithm. The foil in the lowermost region of interest (Figure 1) has significantly lower contrast and is much less distinct than the other regions. Consequently the frame-by-frame displacements ($D(o)$, Equation 1) and associated length changes are noisy and the fitted sinusoidal length change is poorly constrained using the previous algorithm (red line, Figure 3c). The new algorithm, on the other hand,

returns well constrained phases and amplitudes from the noisy data (Figure 3c). This is because the SSD (D) values at the highest offsets (o) constrain the fit. Despite the improvements, only the top marker foil was used in the following analysis, due to the smaller errors.

Sample strain caused by the sinusoidal deformation is defined as:

$$\varepsilon = A/\bar{l} \tag{7}$$

where A is the amplitude of the sinusoidal length variation and $\bar{l}$ is the mean length of the sample (Equation 3) after removing the sinusoidal deformation. In some cases, the background strain in the sample is of comparable magnitude to, or even larger than, the sinusoidal strain amplitude (e.g. Figure 3b); in the subsequent analysis this bulk change is ignored.

4 Anelastic model

Assuming that the corundum standard is elastic and isotropic, the frequency-dependent Young's modulus of the zinc sample is:

$$E_{\mathrm{Zn}} = \frac{\varepsilon_{\mathrm{Al_2O_3}}}{\varepsilon_{\mathrm{Zn}}} E_{\mathrm{Al_2O_3}} \tag{8}$$

where ε is the sinusoidal strain amplitude (Equation 7) in each sample and $E_{\mathrm{Al_2O_3}}$ is the elastic Young's modulus of corundum. The Young's modulus of corundum, $E_{\mathrm{Al_2O_3}}$, was calculated as the Voigt-Reuss-Hill average of corundum's elastic stiffnesses (c_{ij}s), at the temperature of the thermocouple and the pressure calculated from the diffraction. These calculations were done using MSAT [*Walker and Wookey*, 2012] and the same elastic stiffnesses used to determine the pressure [Section 2.4, *Gieske and Barsch*, 1968; *Goto et al.*, 1989].

The strain energy dissipation is:

$$Q^{-1} = 1/\tan^{-1}(\Phi_{\mathrm{Al_2O_3}} - \Phi_{\mathrm{Zn}}) \tag{9}$$

where $\Phi_{\mathrm{Al_2O_3}}$ and Φ_{Zn} are the phase of the length changes in the corundum standard and zinc sample respectively.

The temperature and oscillation period variation in Young's modulus and attenuation can be fit with various models of linear viscoelasticity [Figure 4, e.g. *Sundberg and Cooper*, 2010; *Nowick and Berry*, 1972; *Jackson et al.*, 2000; *Faul and Jackson*, 2015; *Jackson*, 2015]. Each model has different characteristic frequency-dependent behaviour that relates the stress, $\sigma(t) = \sigma_0 \exp(i\omega t)$ where $\omega = 2\pi f$, to the strain response, $\varepsilon(t) = \varepsilon_0 \exp(i\omega t - \delta)$, by a loss angle, δ. For each model, the strain response can be obtained by

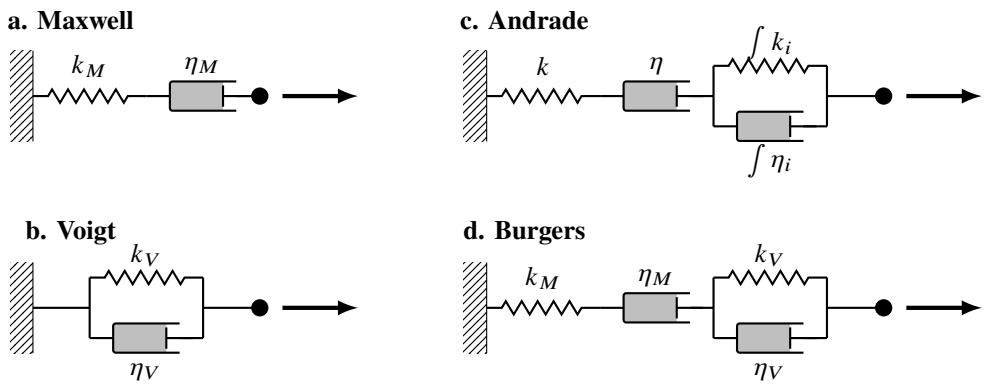

Figure 4. Schematic representations of (a) Maxwell, (b) Voigt, (c) Andrade and (d) Burgers models of anelasticity. Springs (labelled k) represent the elastic components of the model and dashpots (labelled η) the viscous components; under uniaxial deformation $k_M \equiv E$, the Young's modulus. Dynamic compliances (Equation 10) of the Maxwell, Andrade and Burgers models are presented in Equations B.2, C.3 and 15 respectively.

integrating its behaviour over the stress history to compute the dynamic compliance, $J^*(\omega)$ [*Nowick and Berry*, 1972; *Jackson*, 2015]:

$$J^*(\omega) = \frac{\varepsilon(t)}{\sigma(t)} = \mathrm{i}\omega \int_0^\infty J(t)\exp(-\mathrm{i}\omega t)\mathrm{d}t \tag{10}$$

Separating the instantaneous (elastic, real) and retarded (viscous or anelastic, imaginary) parts gives:

$$J^*(\omega) = J_1(\omega) - \mathrm{i}J_2(\omega) = J_U + \mathrm{i}\omega \int_0^\infty [J(t) - J_U]\exp(-\mathrm{i}\omega t)\mathrm{d}t \tag{11}$$

where J_U is the unrelaxed compliance and the inverse of the elastic modulus ($J_U = 1/M$). For simple shear torsion experiments, the relevant elastic modulus is the shear modulus (μ) and for the uniaxial deformation experiments performed here, M is the Young's modulus (E).

The frequency-dependent elastic modulus ($M = E$ or μ) can be determined from the expressions for J_1 and J_2:

$$M(\omega) = [{J_1}^2(\omega) + {J_2}^2(\omega)]^{-1/2} \tag{12}$$

and the associated strain energy dissipation is:

$$Q^{-1}(\omega) = \frac{J_2(\omega)}{J_1(\omega)}. \tag{13}$$

Each viscoelastic dissipation model has different characteristic behaviour and equations. For the Burgers model (Figure 4d) these equations are usually expressed in terms of

$J_M (= 1/k_M \equiv 1/E_M)$, $J_V (= 1/k_V \equiv 1/E_V)$, η_M and τ_V, where τ is a relaxation time:

$$\tau = \eta/k \equiv \eta/E \tag{14}$$

Separating the independent components simplifies the fitting of models to data. The complex compliance, written in terms of the four independent model components, is [after *Faul and Jackson*, 2015]:

$$J^*(\omega) = \frac{1}{E_M} + \frac{1}{E_V(1 + \mathrm{i}\omega\eta_V/E_V)} - \frac{\mathrm{i}}{\omega\eta_M}$$

which rearranges to:

$$J_1(\omega) = \frac{1}{E_M} + \frac{1}{E_V(1 + \omega^2\eta_V^2/E_V^2)} \tag{15a}$$

$$J_2(\omega) = \frac{\omega\eta_V}{E_V^2(1 + \omega^2\eta_V^2/E_V^2)} - \frac{1}{\omega\eta_M} \tag{15b}$$

where E_M and E_V are the respective spring constants of the Maxwell and Voigt components of the Burgers model and η_M and η_V are the corresponding dashpot viscosities. The equivalent complex compliance expressions for the Maxwell and Andrade models are in Appendices B and C respectively.

The experimental Young's moduli and Q^{-1} data (Equations 8 and 9) were fit with a two-component Maxwell and four-component Andrade and Burgers models of anelasticity. There is not sufficient density or range of frequencies in this study's data to fit more complex viscoelastic models, e.g. a generalised Burgers model with its normalised distribution of anelastic relaxation times [e.g. *Anderson and Minster*, 1979]. The data at each temperature was fit independently by simultaneously minimising the unweighted normalised residuals for both $E(\omega)$ and $Q^{-1}(\omega)$ (Equations 12 and 13). The parameters solved for in the fitting were the elastic (E) and viscous (η) components of the anelastic models (Equation 15). This ensures, as far as possible, that the model parameters are independent of each other, which is not the case when the relaxation time, τ (Equation 14), is one of the fitted parameters.

By assuming negligible pressure derivatives and a functional form for the temperature dependence of each model parameter, it was possible to simultaneously fit all the data for each experiment with a Burgers model of anelasticity. A linear temperature dependency was assumed for E_M. The viscosities (η_M and η_V) were assumed to have Arrhenius temperature dependencies ($\ln \eta(T) = a + b/RT$). The temperature dependence of E_V was less clear because with a linear temperature behaviour, which is reasonable for an elastic process, the values of E_V become negative at high temperatures. A number of alternative functions were

tested but an Arrhenius temperature dependence was used because it both approximated the data and remained physically reasonable.

5 Results

A number of sinusoidal deformation experiments were performed for this study. The results from the successful experiments were consistent, but in some cases subject to significant scatter, especially in the phase lag (Equation 9). The experiments that failed, or were not consistent, did so because the zinc extruded from the sample space or deformed significantly during compression. Thus, we focus on the results from the two experiments with the least scatter, one of which had a sample of zinc wire and the other zinc powder. The powder experiment was performed at only one end-load (240 kN, 27 short-tons force) whist the wire experiment was performed at two end-loads. The first end-load was the same as the powder experiment; the data from the second end-load were more scattered and are not discussed here. It is not possible to determine how imperfect the experimental geometry of the powder sample is from the radiographs because most of the assembly is obscured by the anvils (Figure 1). The geometry of the powder experiment is more ideal than that of the wire experiment because in the latter the thermocouple tip protrudes slightly into the anvil gap.

5.1 Recovered Microstructures

Interpretation of anelastic dissipation experiments generally assumes a constant microstructure. However, here we observe significant differences between the initial and recovered microstructures (Figures 5 and 6). Despite very different initial microstructures, the microstructures in the recovered anelasticity samples are remarkably similar.

The recovered anelasticity samples have very similar grain-sizes (Figures 5ci, fi, 6a and b) and Lattice Preferred Orientations (LPOs) (Figures 5cii, fii). The grain-size spread is very similar in both anelasticity samples (Figures 6a and b). The grains in the recovered anelasticity samples are subhedral with some grains having concave boundaries. The samples also contain a small number of quadruple-grain junctions which is consistent with some contribution from grain boundary sliding. The LPO of the two recovered anelasticity samples (Figures 5cii and fii) is dominated by a weak $[0001]$ maxima aligned in the direction of the applied stress and girdles in the orthogonal directions (e.g. $[10\bar{1}0]$, $[2\bar{1}\bar{1}0]$). This is consistent with but not proof of slip of dislocations along the basal plane.

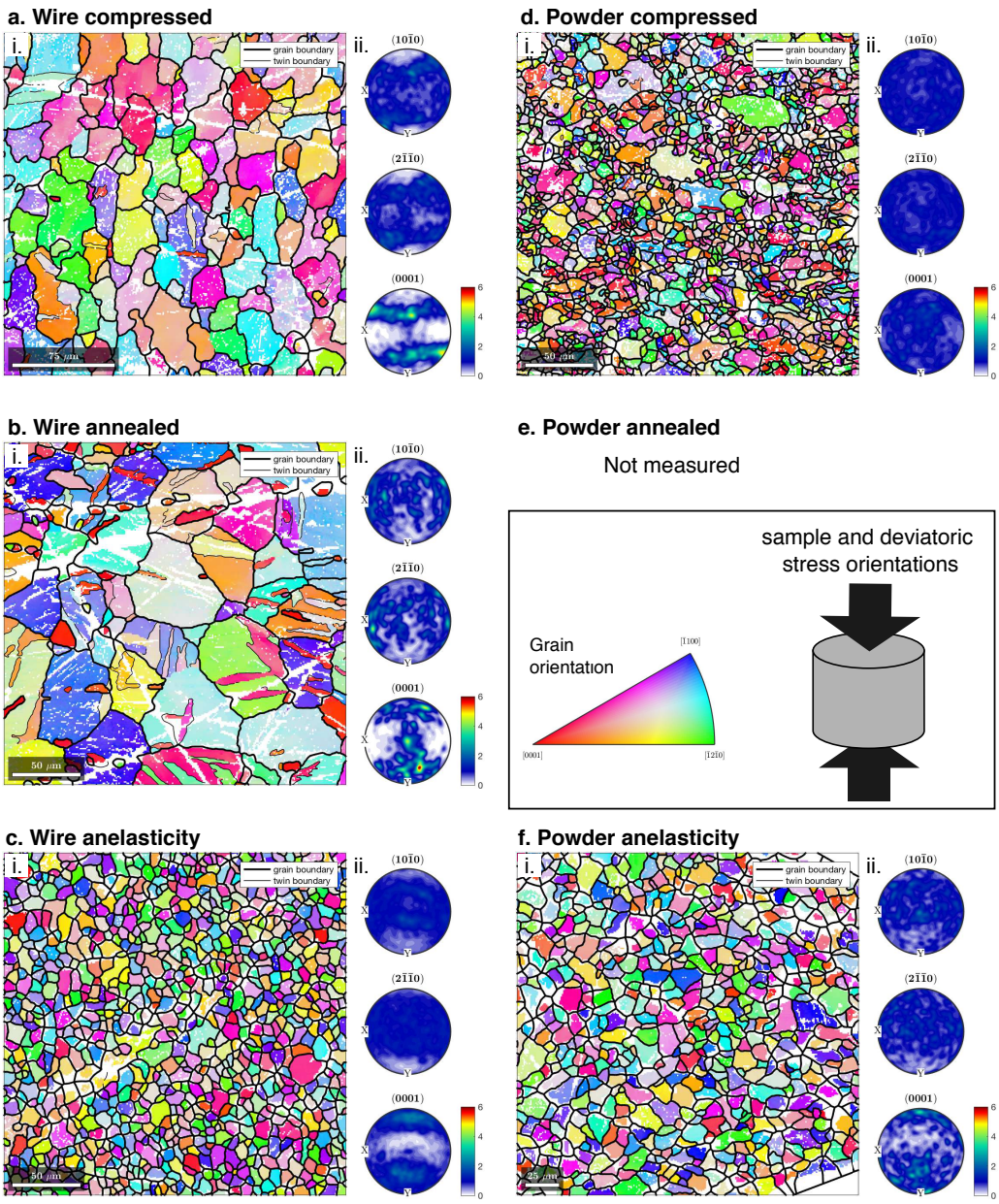

Figure 5. EBSD analysis of the recovered samples. left column (a, b, c,): wire samples; right column (d, e, f): powder samples. Top row (a, d): sample after compression; Middle row (b): samples after annealing for 4 hours and Bottom row (c, f): samples after anelasticity experiments. Parts i. are EBSD maps coloured by Euler angle and parts ii. are upper hemisphere, antipodal pole figures. White areas in the EBSD maps are where the sample was not indexed or data discarded; the linear white features in a and b are scratches from which data were discarded. The sample orientation and applied sinusoidal strain are vertical in the figure, as is the wire drawing direction (a, b, c). All maps and pole figures are on the same colour scale.

These contrast with the grain-size of the compressed and annealed samples. The grain-size of the compressed and annealed wire samples are more than an order of magnitude larger than that of the wire anelasticity sample (Figure 6a). This is despite the apparently large number of small grains in the annealed wire skewing the distribution (Figures 5bi, 6a); the skew is an artefact of scratches in the sample which could not be perfectly accounted for in the grain reconstitution. The mean grain-size of the compressed powder sample is slightly smaller than that of the anelasticity sample (Figure 6b), but the spread of the grain-size is significantly smaller in the anelasticity sample, with fewer small or large grains. The LPO of the compressed wire is very different from that of the annealed or anelasticity samples (Figure 6a), while that of the compressed powder is close to uniform.

The annealed wire sample is abundantly twinned and twins are also present in compressed wire; the cumulative area of twinned grains is plotted in Figures 6a and b. The twin plane of zinc in the annealed wire is calculated to be $\{101\bar{2}\}$. This is consistent with that in the compressed sample and with previous studies of twinning in zinc [e.g. *Antonopoulos et al.*, 1988]. The fractional area of twinned grains is always greater in the annealed wire than in any other sample; something that is also clear in the nearest-neighbour misorientation plot (Figures 6c), where the annealed wire shows significant numbers of grains with misorientations of ~86°. The anelasticity samples show almost no twinning even though twinning is a low-strain deformation mechanism. This is not a grain-size effect; the fractional area of twinned grains is always larger in the compressed or annealed samples than in the anelasticity samples.

The distribution of neighbour-pair misorientation angles are plotted using the method of [*Wheeler et al.*, 2001] and these are very similar for the two recovered anelasticity samples both of which are very different from their initial compressed distributions (Figures 6c and d). At angles greater than 80° twinning affects the non-anelastic samples and the distributions are cut off at the 10° used as the grain boundary threshold. Random-pair distributions for angles less than 80° provide a reference against which the nearest-neighbour misorientations can be compared. Both the compressed samples have significant excesses of low-angle nearest-neighbour pairs relative to the random pair distributions. This is consistent with the presence of dislocations and the continuous accretion of dislocations into sub-grain boundaries to make new grains, so called *'continuous dynamic recrystallisation'*. Both the anelasticity samples have a close correlation between the nearest-neighbour and random-pair

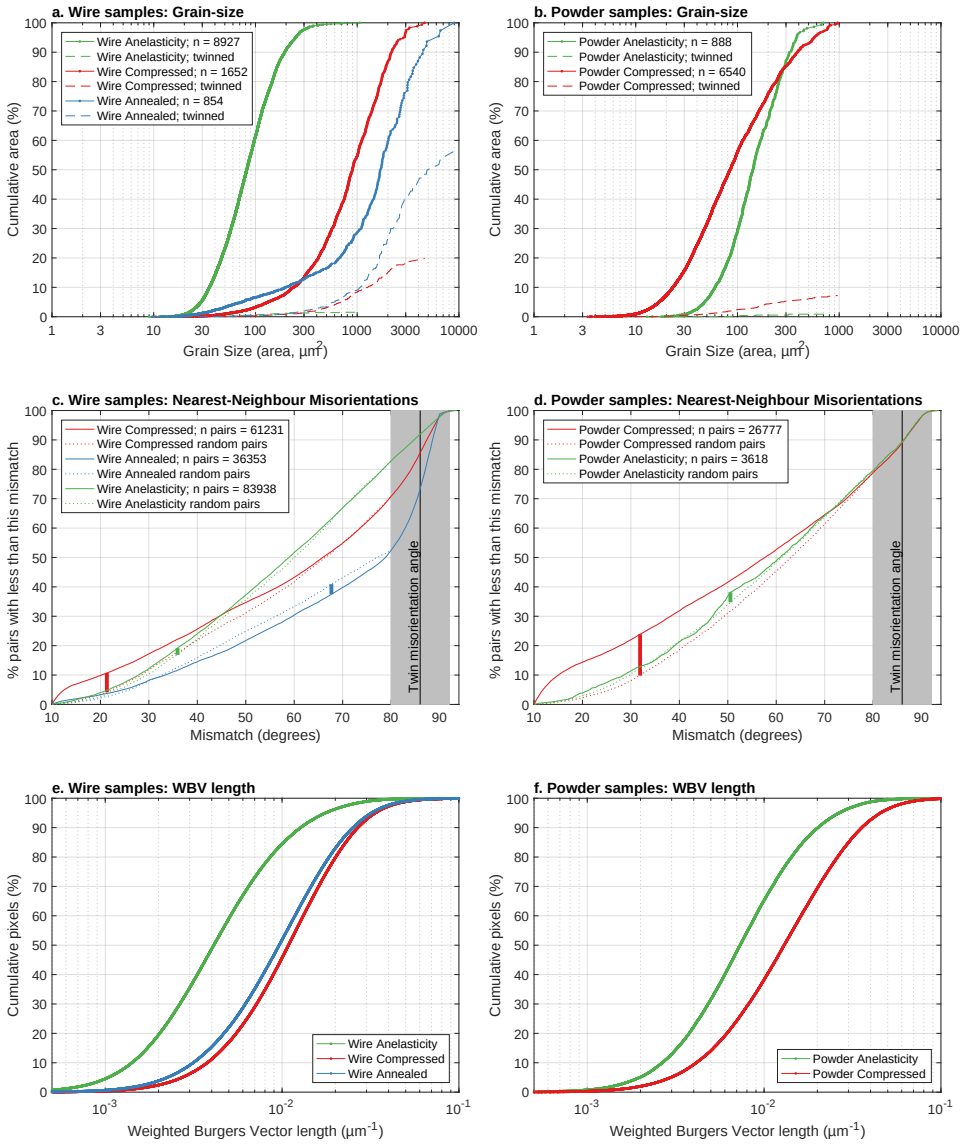

Figure 6. Grain-size (a, b), nearest-neighbour misorientation (c, d) and weighted Burgers vector length (e, f) distributions for the wire (left column) and powder (right column). The dashed lines in a and b are the area of the sample that contains twinned grains. The dashed lines in c and d are the random pair misorientation distributions for the data, the thick bars show the position and size of the largest deviation of the neighbour-pair distribution from that of the random-pair distribution. The solid black lines in c and d show zinc's twin misorientation angle and the gray bar highlights the region influenced by twinning.

misorientation distributions. This implies little or no crystallographic relationship between neighbouring grains.

The weighted Burgers vector length (WBVL) is used as a proxy for dislocation density in the samples that makes no assumptions about the possible slip systems. Figures 6e and f plot the cumulative WBVL distribution for the samples in this study; WBVL maps, of the same areas as shown in Figure 5, are plotted in Supplementary Figure S1. The compressed wire and powder have very similar WBVL values. Annealing of the wire fractionally reduces the WBVL, consistent with dislocations annealing out of the sample. The anelasticity samples though have significantly smaller WBVL than the compressed or annealed samples but the mean WBVL is ~50 % greater in the powder. The anelasticity samples therefore have lower dislocation densities than the other samples.

The differences between samples are unlikely to be caused by noise in the EBSD data because the WBVL is not uniformly distributed (Figure S1), as would be expected for random noise. Instead it is concentrated in some grains, sub-regions of grains and is in some cases in bands within grains, whilst other grains have consistently low WBVL values. Only few coherent sub-grain boundaries could be identified within the grains; either the grains had no sub-grain boundaries or sub-grain boundaries were identified for almost every pixel. There is no strong orientation of the WBV with respect to the crystallographic directions, indicating that multiple slip systems must have been activated within the samples.

It is unlikely that significant dislocation density annealed out of the anelasticity samples in the time taken for the experiments to cool down after the temperature was quenched. Because (a) both the wire and powder anelasticity samples were at <200 °C when quenched and cooling to <50 °C takes less than a minute, (b) the annealed wire sample retains much greater non-random dislocation density and (c) the deformation micro-structures do not show any indication of annealing (i.e. no grain boundary area reduction, no polygonal foam textures, etc.).

The similarity in the overall fabric of the recovered anelasticity samples coupled with the significant contrast to the other samples indicates that the anelasticity sample fabric has developed during the experiment and is controlled by the experimental conditions. The similarity of the grain-size between the recovered samples, the low dislocation and twin densities combined with the disequilibrium grain shapes implies rapid recrystallisation of the samples during the experiment. This is consistent with the rapid growth and disappearance of peaks

in the zinc diffraction observations and ambient temperature dynamic recrystallisation previously observed in zinc [*Liu et al.*, 2020]. Zinc is highly susceptible to grain growth and at elevated temperatures would ordinarily grain grow very quickly. Therefore, the small grain-size and low dislocation density, is an consequence of the sinusoidal deformation and the process leading to this is likely related to the anelastic response.

5.2 Sinusoidal deformation experiments

The frequency-dependent Young's moduli ($E(\omega)$, Figure 7) and dissipation ($Q^{-1}(\omega)$, Figure 8) of the two samples are listed in Table 1 along with the experimental observations used to calculate them. The typical strains in both the sample ($\sim\ 5 \times 10^{-4}$) and the standard ($\sim\ 1 \times 10^{-4}$) are smaller than the typical strains measured by *Li and Weidner* [2007] but large compared to the strains used in previous low-pressure anelastic measurements [2×10^{-6} – 2×10^{-5}, e.g. *Jackson et al.*, 2000]. The corundum strain implies uniaxial stress amplitudes ranging from 111 to 374 MPa, with a mean of 241 MPa. These stresses, the comparatively large value of Q^{-1} in these experiments (Figure 8) and the decreases in E_M (Figure 7) indicate that the samples could be outside of the linear elastic regime.

Outside of the linear anelastic regime, large stresses decrease the values of $E(\omega)$ and increase $Q^{-1}(\omega)$ [e.g. *Li and Weidner*, 2007], which is consistent with the observations here. The large stresses will enhance creep in the samples, thus providing a lower bound for $E(\omega)$ and an upper bound for $Q^{-1}(\omega)$.

The data show a decrease in Young's modulus and increase in dissipation with oscillation period, as expected for a sample with viscoelastic behaviour (Figures 7a,b). The change in $E(\omega)$ and $Q(\omega)^{-1}$ with temperature and oscillation period is greater in the wire (Figures 7a and 8a) than in the powder (Figures 7b and 8b). The $E(\omega)$ data are predominantly smaller than the isotropic average elastic Young's moduli, here defined as the average of a uniform random distribution of zinc crystal orientations (solid black lines in Figure 7). All the data fall between the maximum and minimum possible Young's moduli of zinc, which are defined here as the maximum and minimum possible moduli for variation in the straining direction of a zinc single crystal (dashed black lines in Figure 7). The zinc Young's moduli were calculated in MSAT [*Walker and Wookey*, 2012] using the ambient condition and temperature dependencies of the elastic stiffnesses (c_{ij}s) of *Alers and Neighbours* [1958] and the pressure derivatives of *Srinivasan and Rao* [1971] as compiled by *Ledbetter* [1977].

There is no significant offset between the data collected before and after the maximum temperature in each experiment (open vs. filled symbols in Figures 7 and 8; Table 1 lists the data in order of collection). The relatively large change in pressure between the first and last data sets (Table 1) has no discernible effect on the data implying pressure derivatives close to zero.

For a sample with constant radial stresses, increasing the uniaxial stress by n MPa increases the pressure by $1/3n$ MPa. If the confining force is constant in our experiments, pressure varies from peak to trough over the stress cycle by an average of 320 MPa; a value that is smaller than the typical error on the pressure measurement. If the pressure is changing during the experiment, strictly, any measurement of Young's modulus attenuation is convolved with that of the bulk modulus. However, we do not think this effect is significant here because: (a) volume compression is a purely elastic process, and (b) the experimental protocol utilised here, has been shown elsewhere, to maintain the pressure in solid-media apparatus approximately constant to very high strains [*Hunt et al.*, 2014]. Note that any measurement of Young's modulus at finite strain (e.g. nano-indentation, tension) suffers from the same convolution of stress and pressure as our experiments.

Fitting the data with a Maxwell (Equation B.2) or Andrade (Equation C.3) model did not produce reasonable fits to the data. Neither model can reproduce the gradient changes in the dissipation data with frequency (Figure 8a) and the best fitting Maxwell model requires a frequency-dependent viscosity. The Andrade model fit prefers the micro-creep coefficient (n, Equation C.3) to be > 200. This is much greater than the generally accepted value of $n \sim 1/3$ garnered from micro-creep data [e.g. *Sundberg and Cooper*, 2010] and which has also been observed in creep of zinc [*Cottrell and Aytekin*, 1947]. The Burgers model (Equation 15), on the other hand, produces a reasonable fit to the data and captures its major features, specifically the decrease in $E(\omega)$ with temperature and period as well as the shape of the dissipation data. The Burgers model parameters calculated independently at each temperature are plotted in Figure 9 and listed in Table 2. The extent of the data in frequency is not sufficient to reasonably fit an extended Burgers model [e.g. *Jackson*, 2015]. However, the extended Burgers model predicts that the modulus (here E) varies smoothly with frequency but here there is evidence of a distinctly non-linear change.

Assuming temperature dependencies for each Burgers model parameter enables a single model to be fit to all the data from each experiment. The models are plotted with the

Group	Temperature (°C)	Pressure (GPa)	Period $1/f$ (s)	Strain Amplitude Zinc ($\varepsilon \times 10^6$)	Strain Amplitude Al_2O_3 ($\varepsilon \times 10^6$)	Phase Lag $\Phi_{Al_2O_3} - \Phi_{Zn}$ (degrees)	$E_{Al_2O_3}$ (GPa)	$E_{Zn}(\omega)$ (GPa)	$Q^{-1}(\omega)$
Zn_02, Wire Sample									
1	25	4.8±0.8	299.9 ± 1E-08	687 ± 3E-03	188 ± 4E-03	12.4 ± 2E-04	425.4	116.7 ± 3E-03	0.67 ± 6E-05
			100.4 ± 0.001	658 ± 4	198 ± 5	4.3 ± 0.5		127.9 ± 16.0	0.74 ± 0.14
			30.0 ± 0.003	545 ± 2	168 ± 2	4.8 ± 1.2		130.8 ± 31.3	0.73 ± 0.30
			10.0 ± 0.002	261 ± 1	84 ± 2	5.5 ± 1.8		137.9 ± 46.0	0.72 ± 0.47
2	100	4.8±0.8	299.4 ± 9E-09	784 ± 2E-03	172 ± 3E-03	20.5 ± 3E-04	422.5	92.9 ± 2E-03	0.66 ± 6E-05
			100.0 ± 0.001	693 ± 6	175 ± 7	9.6 ± 0.8		106.5 ± 10.0	0.68 ± 0.20
			30.2 ± 0.005	554 ± 3	167 ± 3	6.5 ± 1.3		127.5 ± 26.0	0.71 ± 0.33
			30.1 ± 0.003	558 ± 2	164 ± 2	7.0 ± 0.9		123.8 ± 16.2	0.70 ± 0.23
			10.0 ± 0.002	264 ± 2	84 ± 2	4.4 ± 1.7		133.8 ± 51.6	0.74 ± 0.45
3	200	4.2±0.4	299.8 ± 7E-09	872 ± 2E-03	194 ± 2E-03	17.4 ± 2E-04	414.7	92.5 ± 1E-03	0.66 ± 4E-05
			100.1 ± 0.001	820 ± 3	183 ± 3	11.0 ± 0.3		92.7 ± 3.3	0.68 ± 0.08
			29.9 ± 0.004	645 ± 3	145 ± 3	9.6 ± 1.6		93.4 ± 15.5	0.68 ± 0.39
			10.0 ± 0.002	300 ± 2	79 ± 2	7.2 ± 2.0		109.8 ± 31.2	0.70 ± 0.51
4	300	4.2±0.4	300.0 ± 2E-08	882 ± 2E-03	164 ± 3E-03	19.7 ± 2E-04	409.4	-	0.66 ± 5E-05
			100.9 ± 0.002	840 ± 4	125 ± 9	21.5 ± 1.7		61.0 ± 6.6	0.66 ± 0.40
			29.9 ± 0.003	675 ± 2	108 ± 3	13.1 ± 2.1		65.5 ± 10.8	0.67 ± 0.51
			10.0 ± 0.002	308 ± 1	66 ± 3	-6.9 ± 2.8		87.4 ± 3.6	-
5	400	4.1±0.6	299.8 ± 4E-08	928 ± 8E-03	96 ± 1E-02	23.2 ± 2E-03	403.5	41.7 ± 6E-03	0.65 ± 4E-04
			99.4 ± 0.001	875 ± 5	92 ± 8	17.9 ± 1.8		42.4 ± 5.6	0.66 ± 0.42
			30.0 ± 0.003	712 ± 2	89 ± 4	18.7 ± 2.5		50.4 ± 7.1	0.66 ± 0.60
			10.0 ± 0.002	331 ± 2	55 ± 3	11.6 ± 3.2		67.2 ± 19.0	0.67 ± 0.78
6	250	3.4±0.6	300.8 ± 2E-08	850 ± 7E-03	127 ± 9E-03	17.3 ± 1E-03	408.2	61.2 ± 5E-03	0.66 ± 2E-04
			99.9 ± 0.001	823 ± 4	142 ± 5	18.6 ± 0.7		70.4 ± 3.6	0.66 ± 0.17
			33.5 ± 0.063	580 ± 11	114 ± 14	9.9 ± 8.5		80.0 ± 69.2	0.68 ± 2.07
			10.0 ± 0.002	307 ± 2	75 ± 3	11.9 ± 2.3		100.4 ± 19.7	0.67 ± 0.56
7	150	3.3±0.9	301.4 ± 1E-08	800 ± 1E-02	184 ± 2E-02	14.0 ± 1E-03	412.8	94.8 ± 1E-02	0.67 ± 2E-04
			100.3 ± 0.001	764 ± 10	186 ± 10	10.0 ± 0.9		100.6 ± 10.9	0.68 ± 0.23
			30.0 ± 0.004	638 ± 4	152 ± 4	8.6 ± 1.7		98.4 ± 19.8	0.69 ± 0.42
			10.0 ± 0.002	308 ± 3	89 ± 3	6.4 ± 2.1		119.5 ± 40.0	0.71 ± 0.54
Zn_08, Powder Sample									
1	28	2.6±0.6	10.0 ± 0.001	272 ± 3	79 ± 3	2.9 ± 2.2	415.3	121.0 ± 91.6	0.81 ± 0.61
			30.0 ± 0.002	575 ± 3	158 ± 3	5.3 ± 1.2		114.2 ± 26.7	0.72 ± 0.32
			99.9 ± 0.012	692 ± 4	191 ± 3	5.6 ± 1.3		114.8 ± 26.0	0.72 ± 0.32
2	182	3.7±0.7	10.0 ± 0.001	319 ± 3	80 ± 3	8.7 ± 2.3	413.2	103.4 ± 27.8	0.69 ± 0.57
			30.0 ± 0.002	628 ± 3	153 ± 2	10.8 ± 1.2		100.6 ± 11.1	0.68 ± 0.29
			99.5 ± 4E-05	747 ± 55	174 ± 43	10.6 ± 2.8		96.2 ± 34.7	0.68 ± 0.67
3	227	3.6±1.5	10.0 ± 0.001	312 ± 3	75 ± 3	3.2 ± 2.4	410.4	99.0 ± 76.3	0.79 ± 0.67
			30.0 ± 0.002	623 ± 4	134 ± 3	7.7 ± 1.6		88.0 ± 18.2	0.69 ± 0.39
			99.9 ± 0.012	747 ± 4	139 ± 3	13.7 ± 1.7		76.7 ± 9.8	0.67 ± 0.41
4	279	3.7±0.5	10.0 ± 0.001	305 ± 3	74 ± 3	6.1 ± 2.4	408.0	98.4 ± 39.4	0.71 ± 0.61
			30.0 ± 0.002	611 ± 3	131 ± 3	9.6 ± 1.4		87.3 ± 13.2	0.68 ± 0.35
			99.9 ± 0.012	729 ± 4	160 ± 3	9.4 ± 1.6		89.3 ± 15.3	0.68 ± 0.39
5	377	3.4±0.4	10.0 ± 0.001	306 ± 3	66 ± 3	4.3 ± 3.1	401.8	86.7 ± 63.5	0.75 ± 0.82
			30.0 ± 0.002	610 ± 3	120 ± 2	10.8 ± 1.6		78.8 ± 11.8	0.68 ± 0.39
			100.0 ± 0.012	713 ± 4	143 ± 3	-12.4 ± 1.6		80.6 ± 1.8	-
6	34	2.5±0.6	10.0 ± 0.001	270 ± 3	89 ± 3	3.7 ± 2.1	414.6	136.6 ± 76.1	0.76 ± 0.55
			30.0 ± 0.003	554 ± 3	151 ± 3	8.8 ± 1.4		112.8 ± 18.7	0.69 ± 0.36
			100.0 ± 0.003	664 ± 4	186 ± 3	11.4 ± 0.9		116.0 ± 9.5	0.67 ± 0.22
7	256	2.7±3.6	10.0 ± 0.001	285 ± 2	71 ± 2	6.0 ± 2.4	404.8	100.5 ± 40.0	0.71 ± 0.61
			30.0 ± 0.002	562 ± 3	129 ± 2	8.7 ± 1.4		92.7 ± 14.5	0.69 ± 0.33
			100.0 ± 0.007	667 ± 8	166 ± 7	-19.0 ± 2.3		101.0 ± 4.3	-
8	120	2.9±0.8	10.0 ± 0.001	276 ± 3	78 ± 3	3.2 ± 2.5	412.7	116.7 ± 92.9	0.79 ± 0.70
			30.0 ± 0.002	545 ± 3	148 ± 2	4.4 ± 1.2		112.2 ± 30.6	0.74 ± 0.31
			100.1 ± 0.003	658 ± 3	177 ± 3	6.3 ± 0.9		110.8 ± 15.1	0.71 ± 0.22

Table 1. Experimental conditions and strain data from the two experiments in this study. The data for each experiment are presented in the order in which they were collected. The data in Figures 7 and 8 are calculated from this data using Equations 8 and 9. The values of $E_{Al_2O_3}$ are those used in the calculations and were calculated as described in the text. The missing values in the $E(\omega)$ and $Q^{-1}(\omega)$ columns are values that were obviously incorrect and excluded from the subsequent analysis. For Zn_08, the Al_2O_3 strains are those of the 'top' elastic reference (Figure 3), whilst in Zn_02 only one corundum standard was imaged.

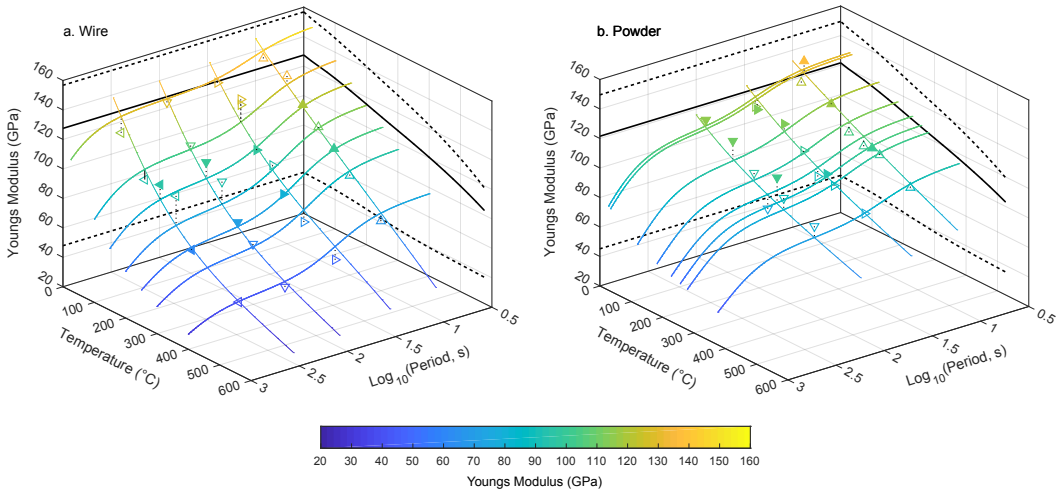

Figure 7. Young's modulus of the Zinc (a) wire and (b) powder samples plotted against temperature and period. The open symbols are the data collected before the maximum temperature of the experiment and the filled symbols after; for the order of the data collection see Table 1. Error bars have been excluded for clarity; the median error in the Young's modulus for both data sets is 10.1 GPa. Dotted lines connect the data to the corresponding point in the fitted plane. The solid lines are the global Burgers model fit to the data and plotted at the nominal periods and temperatures of the measurements. Solid black line in the back planes is the Young's modulus calculated from a Voigt-Reuss-Hill average of the zinc c_{ij}s and the dashed lines are the maximum and minimum possible Young's moduli from the c_{ij}s. All lines terminate at the melting temperature. Note that the directions of the temperature and period axes are reversed relative to Figure 8.

data in Figures 7 and 8. These are a reasonable fit to the data, reproducing its major features. The temperature dependent model parameters are listed in Table 3 along with the functional forms used, and plotted in Figure 9. The global models closely match the parameters calculated independently at each separate temperature.

The dependence of the infinite-frequency Young's moduli (E_M) are approximately linear in temperature (Figure 9a). The values are similar between the two samples and there is some overlap of the individual values. The calculated temperature derivatives (Table 3) are different by more than two standard errors of each other and only the powder sample's temperature derivative is within error of that of the elastic values derived from the stiffnesses ($\mathrm{dE/dT} = -0.07\,\mathrm{MPa\,K^{-1}}$). The values for E_M are all close to the isotropic elastic Young's modulus and within the maximum and minimum bounds.

There are a number of possible causes for the higher-than-expected temperature derivative. Anelastic softening in the corundum standard would increase the apparent tempera-

Group	Temp	Data used				Pressure	Burgers' model parameters				Maxwell time
		Nominal Period (s)					E_M	η_M	E_V	η_V	$\tau = \eta_M / E_M$
	(°C)	10	30	100	300	(GPa)	(GPa)	(10^3 GPa s)	(GPa)	(GPa s)	(s)
Zn_02, Wire Sample											
1	25	y	y	y	y	4.8 ± 0.8	149 ± 6	31.0 ± 2.4	755 ± 58	1551 ± 276	208 ± 16
2	100	y	y	y	y	4.8 ± 0.8	131 ± 5	15.1 ± 1.2	697 ± 58	2855 ± 353	115 ± 9
3	200	y	y	y	y	4.2 ± 0.4	120 ± 6	14.4 ± 1.7	341 ± 38	1503 ± 208	120 ± 14
4	300	E	y	y	Q	4.2 ± 0.4	81 ± 7	11.6 ± 3.7	109 ± 26	1726 ± 301	143 ± 46
5	400	y	y	y	y	4.1 ± 0.6	73 ± 3	5.8 ± 0.6	94 ± 7	595 ± 51	80 ± 8
6	250	y	y	y	y	3.4 ± 0.6	113 ± 18	11.8 ± 4.8	141 ± 39	958 ± 265	105 ± 42
7	150	y	y	y	y	3.3 ± 0.9	125 ± 8	19.3 ± 2.8	369 ± 46	1819 ± 264	154 ± 23
Zn_08, Powder Sample											
1	28	y	y	y		2.6 ± 0.6	126 ± 3	30.9 ± 4.2	790 ± 64	4049 ± 232	246 ± 34
2	182	y	y	y		3.7 ± 0.7	122 ± 7	11.2 ± 2.0	331 ± 37	1125 ± 172	91 ± 16
3	227	y	y	y		3.6 ± 1.5	95 ± 3	8.3 ± 1.9	447 ± 147	3952 ± 345	87 ± 20
4	279	y	y	y		3.7 ± 0.5	106 ± 4	13.0 ± 2.2	352 ± 37	1547 ± 160	122 ± 21
5	377	y	y	E		3.4 ± 0.4	88 ± 8	2.8 ± 5.4	1151 ± 8514	5034 ± 12939	31 ± 61
6	34	y	y	y		2.5 ± 0.6	134 ± 7	15.0 ± 5.8	521 ± 177	3864 ± 450	112 ± 43
7	256	y	y	E		2.7 ± 3.6	112 ± 22	4.1 ± 3.0	791 ± 282	1079 ± 4228	36 ± 27
8	120	y	y	y		2.9 ± 0.8	122 ± 1	19.1 ± 0.5	1070 ± 25	3259 ± 105	157 ± 4

Table 2. Burgers model fits to the data for each temperature conditions. The Data Used columns denote what data was used from each nominal period in calculating Burgers parameters; y – both data used, E - only E, Q - only Q. The data themselves are listed in Table 1. The errors on the values are those reported by the minimisation algorithm used for the fitting.

Constant	Temperature dependency (T, °C)	Intercept (p_0)	Slope (p')
Zn_02, Wire Sample			
E_M	$p_0 + p'.T$	154.6 ± 9.1 GPa	-0.196 ± 0.031 GPa K^{-1}
η_M	$\exp(p_0 + p'/R(T + 273))$	7.6 ± 0.3	6889 ± 1058 J mol^{-1} K^{-1}
E_V	$\exp(p_0 + p'/R(T + 273))$	29.0 ± 2.6	1199 ± 108 K^{-1}
η_V	$\exp(p_0 + p'/R(T + 273))$	5.7 ± 0.4	5331 ± 1385 J mol^{-1} K^{-1}
Zn_08, Powder Sample			
E_M	$p_0 + p'.T$	134.6 ± 10.7GPa	-0.109 ± 0.045 GPa K^{-1}
η_M	$\exp(p_0 + p'/R(T + 273))$	8.4 ± 0.8	3433 ± 2688 J mol^{-1} K^{-1}
E_V	$\exp(p_0 + p'/R(T + 273))$	5.2 ± 0.6	405 ± 259 K^{-1}
η_V	$\exp(p_0 + p'/R(T + 273))$	6.2 ± 0.5	5111 ± 1727 J mol^{-1} K^{-1}

Table 3. Global Burgers model fit to the data listed in Table 1. These fits are plotted with the data in Figures 7 and 8 and compared to the independent temperature fits in Figure 9.

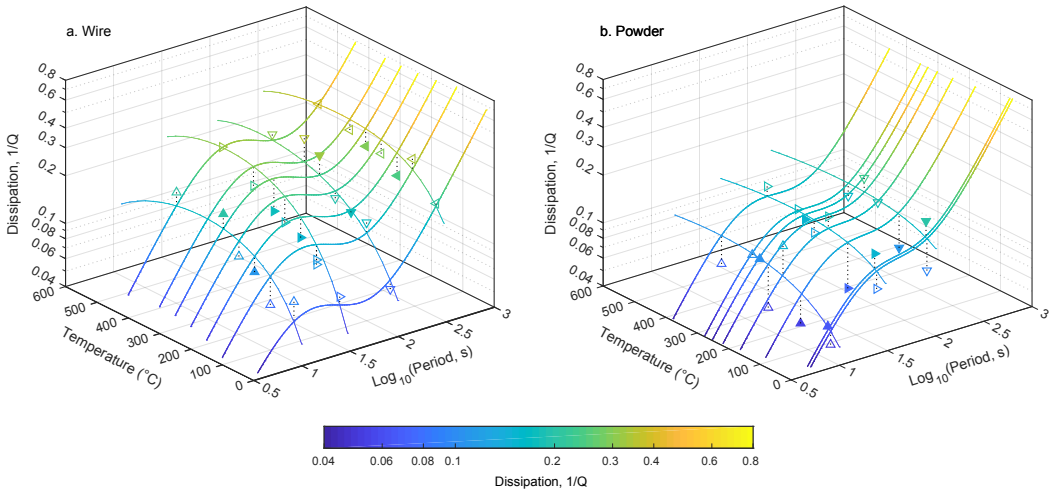

Figure 8. Dissipation in the Zinc (a) wire and (b) power samples plotted on a logorithmic scale against temperature and period. The open symbols are the data collected before the maximum temperature of the experiment and the filled symbols after; for the order of the data collection see Table 1. Error bars have been excluded for clarity. Dotted lines connect the data to the corresponding point in the fitted plane. The solid lines are the global Burgers model fit to the data and plotted at the nominal period and temperatures of the measurements. All lines terminate at the melting temperature. Note that the directions of the temperature and period axes are reversed relative to Figure 7.

ture derivative but this is deemed unlikely to be significant because of the relatively low temperatures and other studies do not observe significant anelastic behaviour in corundum [*Li and Weidner*, 2007]. It is possible geometrical imperfections, such as zinc being partially replaced in the deforming column with the boron nitride sleeve, affect the measurements. Hexagonal Boron nitride has a Young's modulus of ~770 GPa at room temperature and ~620 GPa at 400 °C [*Thomas et al.*, 2017], significantly higher than that of zinc. The Young's modulus measurements are therefore not significantly contaminated with signal from the boron nitride sleeve. Another possibility is that the sampling space of the data skews the calculated values but this cannot be tested here.

The creep viscosities (η_M, Figure 9b, Table 3) are within two standard deviations of each other and exhibit an Arrhenius relationship between viscosity and inverse temperature. The viscosities have similar magnitude, between 100 and 200 °C, to values from creep experiments on high-purity zinc by *Murthy and Sastry* [1982] and *Tegart and Sherby* [1958], although they reduce with temperature much more slowly. The activation energies for creep in the wire and powder are 6.8±1.1 and 3.4±2.7 kJ/mol respectively. They are much smaller

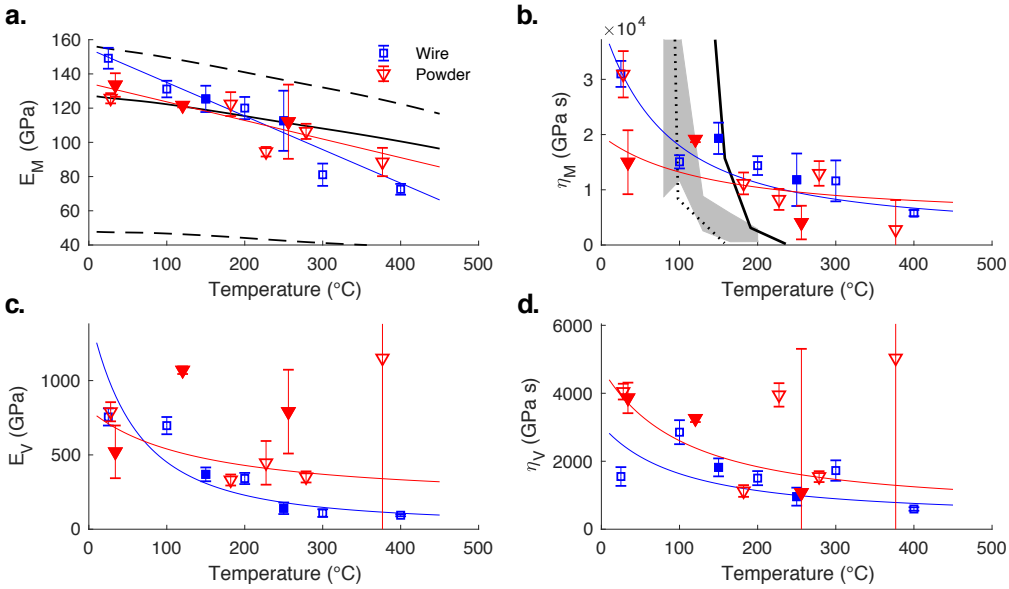

Figure 9. Burgers model parameters plotted against temperature. The symbols are the Burgers fit to the data at each temperature only; the blue squares denote the wire sample and the red triangles are for the powder sample. The open symbols are the data collected before the maximum temperature of the experiment and the filled symbols after. Red and blue lines are from the fit to all the data assuming the temperature derivatives listed in Table 3. In a) the solid black line is the isotropic elastic Young's modulus of zinc at the average pressure of the wire experiment (4.1 GPa), the dashed lines are the maximum and minimum possible elastic Young's moduli calculated in MSAT [*Walker and Wookey*, 2012]. In b) the solid black line, dashed black line and grey area are viscosities ($\eta = \sigma/\dot{\varepsilon}$) derived from the experiments in dislocation-controlled creep regimes by *Tegart and Sherby* [1958], *Thompson* [1955] and *Murthy and Sastry* [1982] respectively. There are no comparable previous measurements for parts c. and d.

than the activation energies for creep by dislocation climb or basal slip in zinc [88 and 159 kJ/mol respectivley, *Tegart and Sherby*, 1958] or implied by the creep data of *Murthy and Sastry* [1982]. The values here are also significantly smaller than the activation energy for zinc self-diffusion [91.3 - 101.7 kJ/mol, *Chabildas and Gilder*, 1972; *Shirn et al.*, 1953] or grain boundary diffusion [60.7 kJ/mol, *Wajda*, 1954]. Twinning can produce strains of up to 7 % in zinc [*Price*, 1961], but the activation energy is 29.7±10 kJ/mol [*Cooper and Washburn*, 1967] and not many twins are observed in the anelasticity samples. Grain boundary sliding has a wide range of activation energies; ranging from $40 - 100$ kJ/mol in zinc bicrystals [*Watanabe et al.*, 1984], to as low as 20 kJ/mol [*Matsunaga et al.*, 2010]. The lowest activation energies are for grain boundary sliding and they are still significantly greater than those observed here.

The functional forms of the Voigt elements of the model are less clear and more scattered than those of the Maxwell elements. For both elements an Arrhenius temperature dependence was assumed because other functional forms gave unphysical results or did not describe the data well. The values of the two parameters are similar between the experiments but those from the powder sample tend to be slightly greater than from the wire sample. The value of η_V is an order of magnitude less than that of η_M. Conversely, at all temperatures, the values of anelastic spring component (E_V) are much greater than the pure elastic component (E_M).

The global model of attenuation (Figure 8) reveals differences between the data sets. In the wire's Q^{-1} values, there are two clear inflection points at each temperature (i.e. $[\partial Q^{-1}/\partial \text{Period}]_T = 0$) within the range of experimental periods (Figure 8a). The position of these inflection points, and therefore the dissipation peak, increases by about 0.25 log-units with increasing temperature. The steepest gradients in $[\partial E/\partial \text{Period}]_T$ correspond to this same period region (Figure 7a). The powder sample does not have such a prominent dissipation peak and the position of the minimum gradient decreases in period slightly with increasing temperature (Figure 8b). The corresponding change in Young's modulus is also less pronounced than in the wire (Figure 7b). There is also more variation in $[\partial Q^{-1}/\partial T]_{\text{Period}}$ and $[\partial E/\partial T]_{\text{Period}}$ in the wire than the powder. This points to subtle differences between the experiments. They are likely due to imperfections in sample geometry, rather than systematic differences between the samples, and not significant for interpretation of the experiments.

In this study, the interpretation of the data is restricted by the number of periods at which the data was collected and the scatter in the data. Small geometrical imperfections, while possibly influencing the details of the measurements, do not appear to significantly distort the overall picture. The overall similarity of the Burgers model parameters and the microstructures of the two samples implies the same physical process is causing the attenuation in both samples. The sample histories (i.e. wire vs. powder) have a small but distinguishable effect on the measurements.

6 Discussion

The similarity of the recovered microstructures and Burgers models for both the wire and powder samples strongly supports the dissipation is controlled by the same physical process in both samples. The nature of this process is discussed in Section 6.1 and is followed by its implications for sound velocity (Section 6.2) and their implications for the inner-core (Section 6.3).

6.1 Dissipation mechanism

Dissipation in the samples is related to, or caused by, the sample recrystallisation which overwrites the sample's previous history and maintains a quasi-equilibrium grain-size during the experiments. This is in contrast to creep experiments in which columnar and randomly oriented zinc retained distinct behaviours [*Bergman et al.*, 2018]. The development and maintenance of the small grain-size, in samples that would normally grain-grow very quickly [e.g. *Niessen et al.*, 1963], indicates that the easiest method of anelastic dissipation in these samples involves grain-boundaries. Dissipation by grain boundary sliding is supported by the 4 grain contacts, the lower and unusually homogeneous WBVL values as well as by the differences in LPO and misorientations which are much closer to a random ODF in the anelastic samples relative to the compressed samples. LPOs which are near random and unusually homogeneous dislocation density is more indicative of grain boundary sliding than dislocation creep. Elastically accommodated grain boundary sliding has been shown to produce a grain-size dependent dissipation peak at a single frequency, at least in a 2-dimensional idealised model [e.g. *Lee and Morris*, 2010]. The presence of a single dissipation peak is supported by the better fit of the Burgers model compared to the Andrade model, which has a wide dissipation peak. In the model of elastically accommodated grain boundary sliding the relaxation time, τ, is linearly dependent on the grain-size, d, according to *Faul and Jackson*

[2015]:

$$\tau = \eta_{gb} d / G\delta \tag{16}$$

where η_{gb} is the grain boundary viscosity, G the elastic shear modulus and δ the grain boundary width. Accordingly, and if applicable, larger grain-size increases the effective creep viscosity of the sample.

It is apparent in this study that the application of stress is forcing the recrystallisation, and the resulting grain-size is such that τ and the associated dissipation peak are within the frequency range of the experiments (Table 2). Whilst this could be entirely coincidental, it is also possible that the grain-size in each measurement changes slightly to minimise the stored energy and thus maximise the dissipation. If this is the case, then the microstructure, at high temperatures, evolves to keep the relaxation time close to that of the driving period. For both samples, the Maxwell time shows a decreasing trend with temperature.

Grain boundary sliding is a significant mechanism in the deformation of columnar zinc [*Bergman et al.*, 2018]. In high-strain experiments on untextured samples, grain boundary sliding only forms a small part of the total strain and appears to saturate with increasing total strain and temperature [*Gokhale et al.*, 2019; *Matsunaga et al.*, 2010]. Geometric misalignment from grain boundary sliding can be accommodated elastically or by dislocations and diffusion. The presence of domains with higher dislocation densities may suggest that grain boundary sliding is accommodated by dislocation creep rather than diffusion creep but we cannot be sure of their relative importance.

Zinc has a high stacking fault energy [*Harris and Masters*, 1965] and would normally undergo recrystallisation by *'continuous dynamic recrystallisaion'* [*Gourdet and Montheillet*, 2003; *Montheillet and Jonas*, 2003] where dislocations aggregate to form subgrain-boundaries and then high angle grain boundaries. In the anelasticity samples, there are relatively few grains with coherent subgrain boundaries and the grain boundary misorientation distributions (Figures 6c–d) are close to the random distribution indicating there is little or no crystallographic inheritance between grains. Additionally, many grains have very low WBVl values, indicating low dislocation density. Grains with the highest WVBL (i.e. dislocation density) have a wide spread of WBV orientations pointing to multiple active dislocation systems. As grains grow and multiple dislocation systems are activated, these are likely to tangle strain-hardening the grains. In order for easy grain boundary dissipation and lower elastic strain energy, new grains are therefore nucleated and grow, so-called *'discontinuous*

dynamic recrystallisation' [*Montheillet and Jonas*, 2003; *Tutcuoglu et al.*, 2019; *Liu et al.*, 2020]. These new grains nucleate randomly and have no inheritance to the grains they ultimately replace.

Grain boundary sliding is also often associated with diffusion in viscoelastic models [e.g. *Cooper*, 2002]. Diffusion is significant on the time scale of the experiment. The platinum marker foils adjacent to the zinc noticeably thicken and blur into the zinc sample, during the experiments, while the thickness of the foils away from the zinc remains constant. The platinum foils double their apparent thickness over the course of the experiments. Using the self-diffusivity of zinc (D) from *Shirn et al.* [1953], the diffusion length ($\sqrt{Dt}$) in zinc is greater than the grain radius at temperatures above ~90 °C, and greater than the radius of the largest grains above ~115 °C. Thus, even in the 10 s period experiments, diffusion is significant and could reasonably be the deformation mechanism – although this is not reflected in the activation energy for the macroscopic creep viscosity (η_M) measured in the experiments. However, the unphysical fit of the Andrade model to the data means that the diffusion is unlikely to be a significant cause of accommodation.

We conclude therefore, that dissipation during the sinusoidal deformation is caused by the combination of dynamic recrystallisation and grain boundary sliding. This prevents the growth of large crystals and instead establishes a quasi-equilibrium grain-size which is constantly reforming. While both diffusion and dislocations may play a role in the dissipation, their magnitude is small compared to that of grain boundary sliding. The establishment of a steady-state grain-size and fabric here is similar to the steady-state foliation that occurs in natural rocks [*Means*, 1981] and implies an overall balance between the grain boundary and internal energy of the grains.

6.2 Anelastic modification of sound velocity

The experiments here show significant softening in zinc at seismic frequencies ($1 \times 10^{-3} \lesssim f \lesssim 1$ Hz) which will reduce the sound velocity. Calculation of $v_P(\omega)$ and $v_S(\omega)$ in an isotropic medium requires knowledge of both the shear modulus and Young's moduli (or two pieces of equivalent information). Here though, we have only measured the frequency-dependent Young's modulus, and fitted for the infinite-frequency, elastic, Young's modulus, E_M (Equation 15, Figure 9a, Table 3). Although, the bulk modulus (K) is also formally anelastic in an anelastic system [*Anderson*, 1989; *Nowick and Berry*, 1972], we assume here

the effective bulk modulus is unaffected by the dissipation mechanism. This is a reasonable assumption because recrystallisation, grain boundary sliding or the presence of dislocations should not significantly affect the compressibility. As additional confirmation, the 1 Hz bulk moduls of (Mg,Fe)O has been shown to closely correspond to the elastic bulk modulus, away from the iron spin transition [*Marquardt et al.*, 2018]. The elastic bulk modulus (K) gives the second piece of information with which to calculate $v_p(\omega)$ and $v_s(\omega)$ from the following relations:

$$v_p(\omega) = \sqrt{\frac{3K[3K + E(\omega)]}{\rho[9K - E(\omega)]}} \tag{17a}$$

$$v_s(\omega) = \sqrt{-\frac{3KE(\omega)}{\rho[E(\omega) - 9K]}} \tag{17b}$$

where ρ is the density. Assuming a bulk modulus with the same anelastic dissipation as the Young's modulus compounds the softening, making it much more significant and further reducing $v_p(\omega)$ and $v_s(\omega)$.

The sound speed of zinc at finite-frequency is plotted in Figure 10a. The required bulk modulus was calculated using the same elastic stiffnesses as the elastic Young's moduli of zinc (Section 4), at the mean pressure of each experiment (Table 1). The density was calculated using a reference density of $7.12\,\mathrm{g\,cm^{-3}}$, the calculated bulk modulus and the thermal expansion coefficients of *Nuss et al.* [2010]. In calculating the sound speed, we used the measured creep viscosity, η_M. At smaller strains, or larger grain-sizes, it can be expected to have an effectively larger value (Equation 16). Removing the effect of η_M, by setting it to a very large value, has only a small effect: the 300 s period v_s changes by less than $\sim 50\,\mathrm{ms^{-1}}$.

The elastic sound velocities, at the pressures of the experiments, are greater than those reported by *Ledbetter* [1977] whose values are for 0 GPa. The change in velocity with temperature in our powder sample compares very well with the data of *Ledbetter* [1977]. The change of velocity with temperature is greater in the wire sample because the temperature dependence of the elastic Young's modulus is also greater (Figure 9a). Close to melting, both Burgers models predict similar reductions in sound speed as a function of frequency. For a 30 s period, the reductions in v_p are 0.05 and $0.11\,\mathrm{km\,s^{-1}}$ for the wire and powder samples respectively; the corresponding reductions in v_s are 0.11 and $0.17\,\mathrm{km\,s^{-1}}$. These correspond to percentage reductions in sound velocity of 1.4 and 2.6 % for v_p and 7.8 and 8.5 % for v_s.

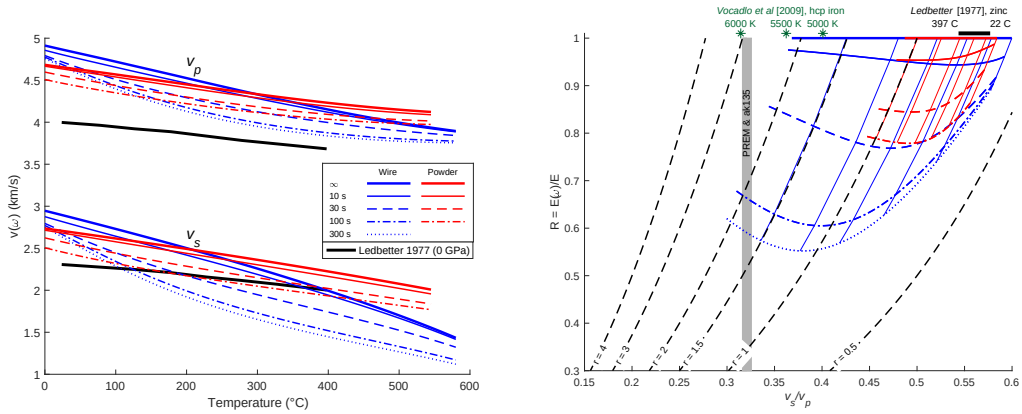

Figure 10. (a) Sound velocity as a function of temperature and experimental wave periods and (b) the relationship between $v_s(\omega)/v_p(\omega)$ against $R = E(\omega)/E$, calculated from the Burgers models and Equations 17 and 20. In both Figures, blue lines denote the wire sample and the red lines the powder sample. Thick black lines are the values from *Ledbetter* [1977]. In (b) the thin blue and red lines are isotherms in the models at 100 °C intervals. The dashed black lines are the relationship denoted by Equation 20 and the green stars are the predicted v_s/v_p ratio from the extrapolated elastic constants of *Vočadlo et al.* [2009]. The grey bar is the range of v_s/v_p values reported by PREM and ak135.

6.3 Effect of anelasticity on the inner-core

The absolute reduction in the zinc's $v_s(\omega)$ is between 1.5 and two times greater than the reduction in $v_p(\omega)$, which in consistent with the inner-core in which $v_s(\omega)$ is reduced more than $v_p(\omega)$ relative to pure Fe at infinite-frequency.

The larger reduction in $v_s(\omega)$ than $v_p(\omega)$ with increased anelastic softening is implied by Equations 17. If we define the bulk modulus to be a multiple of the elastic Young's modulus, i.e.:

$$r = K/E \tag{18}$$

and the amount of anelastic softening as a fraction of the elastic, i.e. infinite frequency, Young's modulus,

$$R = E(\omega)/E, \tag{19}$$

the frequency-dependent sound velocity ratio is:

$$\frac{v_s(\omega)}{v_p(\omega)} = \sqrt{\frac{R}{3r + R}}. \tag{20}$$

The ratio $v_s(\omega)/v_p(\omega)$ is independent of density but implicitly depends on E; an equivalent expression exists in terms of the shear modulus. For real values, $0 \leq R \leq 1$, this relationship

is a maximum at $R = 1$, confirming that under anelastic dissipation v_s reduces faster than v_p. The higher the value of r, the lower the ratio of v_s/v_p in the elastic limit ($R = 1$). At a constant value of anelastic softening (R), the ratio $v_s(\omega)/v_p(\omega)$ changes with temperature via the dependence of r on the elastic stiffnesses.

Figure 10b shows $v_s(\omega)/v_p(\omega)$ against R for $0.5 < r < 4$. It shows that increasing r decreases $v_s(\omega)/v_p(\omega)$ and that increased anelastic softening (Equation 12), decreased R, further reduces $v_s(\omega)/v_p(\omega)$. Any anelastic softening will be accompanied by dissipation (Equation 13); effects that are not accounted for in the plot.

The Burgers models for zinc determined in this study are plotted to illustrate the effects of temperature and anelastic softening (Figure 10b). For both samples, the range of r with temperature is larger than that inferred from the sound speeds of *Ledbetter* [1977]. This is because the change of E_M with temperature is greater than that of the isotropic elastic average (Figure 9a). As with the earlier figures, significantly more softening is observed in the zinc wire than in the powder. Decreases in R at constant temperature (thin red and blue lines in Figure 10b) are accompanied by reductions in $v_s(\omega)/v_p(\omega)$.

Only at the highest temperatures and longest periods does the zinc wire reach the v_s/v_p ratio, but not the absolute velocities, of the inner-core reported by PREM [*Dziewonski and Anderson*, 1981] or ak135 [*Kennett et al.*, 1995]. This is because r is significantly smaller in zinc than in *hcp*-Fe [e.g. *Vočadlo et al.*, 2009]. Although Figure 10b neglects density as a constraint on the composition of the inner-core, it predicts that the inner-core alloy must have $r < 3$ and lower values must be accompanied by finite amounts of anelastic dissipation.

Inner-core sound velocity cannot be matched by the elastic constants of *hcp*-iron [e.g. *Vočadlo et al.*, 2009], which always predict sound velocities that are too fast. However, if anelastic softening is included, the sound velocities can be matched by the elastic constants of *Vočadlo et al.* [2009] with an, admittedly unrealistic, extrapolated temperature of ~7250 K and equally unrealistic $R = 0.68$. Although these conditions match the sound velocity, the density of the hypothetical pure iron remains greater than that of the inner-core. Anelasticity, therefore, does not remove the need for light element(s) in the inner-core and hints that a wider range of light elements could match the inner-core properties than previously has been managed.

Conversely, finite dissipation in the inner-core, reduces seismic wave speed resulting in an underestimation of the inner-core's elastic moduli (K and μ, Equation 20, Figure 10b). The estimated difference between the elastic properties of stiffer pure iron and that of the softer inner-core alloy are therefore overestimated. Thus comparison of seismic wave speed with experimental or computed material properties will tend to over estimate the light element budget of the inner-core and needs to be considered in future studies.

The inner-core is very close to the melting temperature of its alloy and at high temperature iron, like zinc, undergoes rapid recrystallisaion [*Anzellini et al.*, 2013]. Therefore it is likely that the inner-core is undergoing rapid recrystallisation, which we have shown here is an intrinsic part of the dissipation. The stress amplitude of seismic waves is significantly less than those in this study; accordingly any quasi-equilibrium grain-size is expected to be larger in the inner-core than in the experiments here. A larger grain-size will result in less grain boundary area and lower dissipation but even a small amount of anelastic dissipation reduces the effective elastic moduli and reduces the seismic velocity. Regional and depth dependent variations in attenuation [*Pejić et al.*, 2019; *Suda and Fukao*, 1990] may be the result of variation in grain-size and homologous temperature within the inner-core. Directionally dependent attenuation [*Mäkinen et al.*, 2014] could be attributable to shape preferred orientation of crystals giving different directionally dependent effective grain-sizes. It seems unreasonable therefore to be able to fully understand the inner-core without a comprehensive model that accounts for both the seismic velocity and attenuation.

7 Conclusions

Significant dissipation is observed at seismic frequencies in the experiments of this study. This shows that signifcant anelastcity occurs in *hcp* metals at high pressures and temperatures, without the need for a fluid phase or significant impurities. The inner-core also exhibits non-zero Q^{-1} values, evidence of active anelastic processes. Thus anelasticity must be accounted for when interpreting the inner-core's seismic velocity structure.

The high-pressure response of zinc wire and powder samples to sinusoidal stress at seismic frequencies and up to $T/T_M \sim 0.8$ have been measured and show that the *hcp* metal zinc has significant anelastic dissipation at seismic frequencies. The Burgers model used to fit the data successfully reproduces its features. The elastic (E_M) components of the model show a good correspondence to previous studies (Figure 9). The activation energy for creep

(η_M) is much lower than previous studies have found; the values of E_V and η_V are less well constrained and do not simply correspond to a distinct physical process. It is therefore probable that the Burgers model is too simplistic to properly describe the dissipative processes active in the sample but there is not sufficient data to warrant the use of more complex models. The small differences between the experiments are caused by imperfections in the experimental geometry. Nevertheless, the experiments here show that significant anelastic softening occurs at high pressure and temperature in zinc and by extension *hcp* metals.

The recovered samples have very similar grain-size and LPO (Figures 5 and 6a) despite the initial grain-size and fabric being very different. The small amplitude deformation during the experiment appears to have prevented the growth of large grains in both wire and powder samples; the grain-size is therefore in a steady-state fabric, analogous to the steady-state foliation of *Means* [1981]. The grains are not equant equilibrium shapes and have very few dislocations and sub-grain boundaries. It seems likely that the anelastic dissipation is caused by grain boundary sliding combined with dynamic recrystallisation . To the best of our knowledge, this is the first observation of dynamic recrystallisation as a significant contributing factor to an anelastic dissipation mechanism.

Associated with the dissipation is a significant drop in the effective Young's modulus with increasing period and an associated reduction in sound speed. We have shown that anelastic softening reduces $v_s(\omega)$ by more than $v_p(\omega)$. This is consistent with observations of the inner-core, where the reduction in v_s is much larger than that in v_p, relative to pure iron. Accounting for anelasticity and ignoring density, it is possible to match the sound speeds of pure iron to those of the inner-core. Accounting for anelastic reductions of inner-core sound velocity will increase the elastic moduli and sound velocities of the inner-core alloy closer to those of pure iron. Anelastic effects may therefore imply that the light-element budget of the inner-core is less than previously considered. A comprehensive understanding of the inner-core must therefore account for both the seismic velocity and attenuation.

A Temperature Calibration

Thermal gradients in small multi-anvil cells are potentially significant and increase with temperature and distance from the centre of the furnace [*Liebermann and Wang*, 1992; *Hernlund et al.*, 2006]. The corundum standard, which was used to measure the pressure and was the reference to determine the sample's Young's modulus, was not in the centre of the

furnace or immediately adjacent to the thermocouple. A temperature difference between the thermocouple and the corundum standard could result in a systematic underestimation of the Young's modulus of corundum, an error which would propagate into the analysis of anelastic dissipation.

To determine if a significant temperature gradient or difference existed in the experimental cell experiment Zn_06 was performed, in which the temperature was increased until the zinc melted. The temperature at which melting occurs is an independent, absolute, reference of the temperature in the experiment. The cell in this experiment was the same as in the other experiments and the sample was zinc wire. At the same load as before (270 kN), the experiment was heated from 150 °C to ~570 °C over a period of 3 hrs 35 mins, by which point the zinc had melted. During heating, X-radiographs were collected at a rate of 1.5 s/frame. Diffraction patterns were collected intermittently during the temperature ramp.

The melting point of the zinc was determined from the radiographs; when the zinc melted a plume of platinum-rich material rose through the sample. Although the sample melted, it did not make a ball of molten metal in the cell because convection stirred platinum into the sample. There is no eutectic depression of the melting point at the zinc-rich end of the Zn-Pt binary [*Moser*, 1991] and adding platinum to zinc increases the melting temperature and re-froze the sample. The thermocouple temperature was 544 °C when the zinc melted; the error in this measurement is negligible. From the zinc melting curve [$T_{M,0}$ = 419.5°C, $\mathrm{d}T_M/\mathrm{d}P$ = 40 K/GPa; *Errandonea*, 2010] this temperature corresponds to 3.11 GPa.

During heating, the pressure was measured by diffraction from the corundum at 27, 225, 289, 368 and 422 °C. Assuming the temperature in the corundum was the same as the thermocouple reported, the pressures were 3.83(48), 3.52(26), 3.50(15), 3.53(23) and 3.37(34) GPa. A linear fit of the pressure against temperature gives a reduction in pressure of $-1.04\,\mathrm{MPa\,K^{-1}}$ and intercepts the melting curve at 550(13) °C and 3.26(33) GPa. These estimates are within error of the observed melting conditions. Any differences in temperature between the thermocouple, zinc sample and corundum standard are therefore insignificant and no temperature correction is required.

B Maxwell Model

The Maxwell model (Figure 4a) along with the Voigt model (Figure 4b) are the two simplest models that contain intrinsic attenuation and thus frequency-dependent behaviour.

The creep function for the Maxwell model is [e.g. *Faul and Jackson*, 2015]:

$$J(t) = \frac{1}{k_M}(1 + \frac{t}{\tau_M}) \tag{B.1}$$

where the relaxation time $\tau_M = \eta_M / k_M$, k_M is the spring constant and η_M is the dash-pot viscosity. Integrating this creep function over the dynamic compliance (Equation 10) and expressing in terms of k_M and η_M gives [*Faul and Jackson*, 2015]:

$$J^*(\omega) = \frac{1}{k_M}\left(1 + \frac{k_M}{\mathrm{i}\omega\eta_M}\right); \quad J_1 = \frac{1}{k_M}; \quad J_2 = \frac{1}{\mathrm{i}\omega\eta_M}; \quad Q = \frac{k_M}{\omega\eta_M} \tag{B.2}$$

Equation B.2 shows that the Maxwell model's frequency dependence of Q is proportional to period and cannot contain any inflection points (i.e. $d^2Q(\omega)/d\omega^2 \neq 0$).

The Voigt/Kelvin model has Q inversely proportional to period and is also without the possibility of inflection points. The equivalent characteristic equations for which can be found in *Cooper* [2002].

C Andrade Model

The Andrade model (Figure 4c) is a phenomenological model derived from micro-creep experiments and provides a good fit to the transient, pre-steady state, part of creep curves [*Sundberg and Cooper*, 2010; *Cooper*, 2002]. The time-dependent creep function is:

$$J(t) = J_U + \beta t^n + t/\eta, \qquad 1/3 < n < 1/2 \tag{C.1}$$

Integrating this creep function over the dynamic compliance gives [*Faul and Jackson*, 2015]:

$$J^*(\omega) = J_U + \beta\Gamma(1+n)(\mathrm{i}\omega)^{-n} - \mathrm{i}/\eta\omega. \tag{C.2}$$

Rearranging this to the same form as Equation 15, and substituting $J_U = 1/k$, gives:

$$J_1(\omega) = 1/k + \beta\Gamma(1+n)(\mathrm{i}\omega)^{-n}\cos(n\pi/2) \tag{C.3a}$$

$$J_2(\omega) = \beta\Gamma(1+n)(\mathrm{i}\omega)^{-n}\sin(n\pi/2) - \mathrm{i}/\eta\omega \tag{C.3b}$$

where $\Gamma(1+n)$ is the gamma function [*Gribb and Cooper*, 1998] and k, β, n and η are the material properties of the different components of the model (Figure 4c). The parameters β and n describe the shape of the transient seen during creep experiments and under oscillatory stress provide damping over a wide range of frequencies. The value of n has been constrained experimentally to be approximately 1/3 [*Gribb and Cooper*, 1998]. Because dissipation occurs over a wide range of frequencies, the Andrade model has been argued to provide

a physically consistent description of both the rheological and anelastic properties of peridotite [*Sundberg and Cooper*, 2010].

Acknowledgements

S.A.H. (NE/H016309, NE/L006898, NE/P017525), A.M.W (NE/K008803/1 and NE/M000044/1), S.S. (NE/K006290/1) and O.T.L (NE/J018945/1) thank the Natural Environment Research Council (NERC) for funding. Use of the National Synchrotron Light Source (NSLS), Brookhaven National Laboratory, was supported by the U.S. Department of Energy, Office of Science, Office of Basic Energy Sciences, under Contract No. DE-AC02-98CH10886. Use of the X17B2 beamline was supported by COMPRES, the Consortium for Materials Properties Research in Earth Sciences under NSF Cooperative Agreement EAR 10-43050 and by the Mineral Physics Institute, Stony Brook University. Finally we would like to thank Dr Richard Walshaw for his efforts in recommissioning the electron optics facility at Leeds and collecting the last few EBSD data sets under challenging conditions during the pandemic of 2020/21.

The data collected in the course of this study are available from `https://www.bgs.ac.uk/discoverymetadata/13607352.html`.

The 'FoilTrack' package is available from `https://dx.doi.org/10.5281/zenodo.4589219`. The EBSD data is being added to the bgs data repository and will be completed before publication.

References

Alers, G., and J. Neighbours (1958), The elastic constants of zinc between 4.2° and 670 °K, *Journal of Physics and Chemistry of Solids*, *7*(1), 58–64, doi:10.1016/0022-3697(58)90180-x.

Anderson, D. L. (1989), *Theory of the Earth*, Boston: Blackwell Scientific Publications.

Anderson, D. L., and J. B. Minster (1979), The frequency dependence of Q in the Earth and implications for mantle rheology and chandler wobble, *Geophysical Journal International*, *58*(2), 431–440, doi:10.1111/j.1365-246x.1979.tb01033.x.

Aning, A., T. Suzuki, and M. Wuttig (1982), Nonlinear anelasticity of magnesium, *Journal of Applied Physics*, *53*(10), 6797–6808, doi:10.1063/1.330068.

Antonangeli, D., J. Siebert, J. Badro, D. L. Farber, G. Fiquet, G. Morard, and F. J. Ryerson (2010), Composition of the Earth's inner core from high-pressure sound velocity measurements in Fe-Ni-Si alloys, *Earth and Planetary*

Science Letters, *295*(1-2), 292–296, doi:10.1016/j.epsl.2010.04.018.

Antonangeli, D., G. Morard, L. Paolasini, G. Garbarino, C. A. Murphy, E. Edmund, F. Decremps, G. Fiquet, A. Bosak, M. Mezouar, and Y. Fei (2018), Sound velocities and density measurements of solid hcp-Fe and hcp-Fe-Si (9 wt.%) alloy at high pressure: Constraints on the Si abundance in the Earth's inner core, *Earth and Planetary Science Letters*, *482*, 446–453, doi:10.1016/j.epsl.2017.11.043.

Antonopoulos, J., T. Karakostas, P. Komninou, and P. Delavignette (1988), Dislocation movements and deformation twinning in zinc, *Acta Metallurgica*, *36*(9), 2493–2502, doi:10.1016/0001-6160(88)90195-2.

Anzellini, S., A. Dewaele, M. Mezouar, P. Loubeyre, and G. Morard (2013), Melting of iron at Earth's inner core boundary based on fast x-ray diffraction, *Science*, *340*(6131), 464–466, doi:10.1126/science.1233514.

Aubert, J., H. Amit, G. Hulot, and P. Olson (2008), Thermochemical flows couple the Earth's inner core growth to mantle heterogeneity, *Nature*, *454*(7205), 758–761, doi:10.1038/nature07109.

Bachmann, F., R. Hielscher, and H. Schaeben (2010), Texture analysis with MTEX–free and open source software toolbox, *Solid State Phenomena*, *160*, 63–68, doi:10.4028/www.scientific.net/SSP.160.63.

Bachmann, F., R. Hielscher, and H. Schaeben (2011), Grain detection from 2d and 3d EBSD data – specification of the MTEX algorithm, *Ultramicroscopy*, *111*(12), 1720–1733, doi:10.1016/j.ultramic.2011.08.002.

Bazhanova, Z. G., V. V. Roizen, and A. R. Oganov (2017), High-pressure behavior of the Fe-S system and composition of the Earth's inner core, *Physics-Uspekhi*, *60*(10), 1025–1032, doi:10.3367/ufne.2017.03.038079.

Belonoshko, A. B., J. Fu, T. Bryk, S. I. Simak, and M. Mattesini (2019), Low viscosity of the Earth's inner core, *Nature Communications*, *10*(1), doi:10.1038/s41467-019-10346-2.

Bergman, M. I., J. Yu, D. J. Lewis, and G. K. Parker (2018), Grain boundary sliding in high-temperature deformation of directionally solidified hcp zn alloys and implications for the deformation mechanism of earth's inner core, *Journal of Geophysical Research: Solid Earth*, *123*(1), 189–203, doi:https://doi.org/10.1002/2017JB014881.

Cao, A., and B. Romanowicz (2004), Hemispherical transition of seismic attenuation at the top of the Earth's inner core, *Earth and Planetary Science Letters*, *228*(3-4), 243–253, doi:10.1016/j.epsl.2004.09.032.

Caracas, R. (2015), The influence of hydrogen on the seismic properties of solid iron, *Geophysical Research Letters*, *42*(10), 3780–3785, doi:10.1002/2015gl063478.

Chabildas, L. C., and H. M. Gilder (1972), Thermal coefficient of expansion of an activated vacancy in zinc from high-pressure self-diffusion experiments, *Physical Review B*, *5*(6), 2135–2144, doi:10.1103/physrevb.5.2135.

Cooper, R., and J. Washburn (1967), Stress-induced movement of twin boundaries in zinc, *Acta Metallurgica*, *15*(4), 639–647, doi:10.1016/0001-6160(67)90107-1.

Cooper, R. F. (2002), Seismic wave attenuation: Energy dissipation in viscoelastic crystalline solids, *Reviews in Mineralogy and Geochemistry*, *51*(1), 253–290, doi:10.2138/gsrmg.51.1.253.

Cottrell, A. H., and V. Aytekin (1947), Andrade's creep law and the flow of zinc crystals, *Nature*, *160*, 328–329.

Deuss, A. (2014), Heterogeneity and anisotropy of Earth's inner core, *Annual Review of Earth and Planetary Sciences*, *42*(1), 103–126, doi:10.1146/annurev-{E}arth-060313-054658.

Dobson, D. P., S. A. Hunt, L. Li, and D. J. Weidner (2008), Measurement of thermal diffusivity at high pressures and temperatures using synchrotron radiography., *Mineralogical Magazine*, *72*(2), 653 – 658, doi: 10.1180/minmag.2008.072.2.653.

Dobson, D. P., S. A. Hunt, R. McCormack, O. T. Lord, D. J. Weidner, L. Li, and A. M. Walker (2010), Thermal diffusivity of MORB-composition rocks to 15 GPa: implications for triggering of deep seismicity, *High Pressure Research*, *30*(3), 406 – 414, doi:10.1080/08957959.2010.516827.

Dobson, D. P., R. McCormack, S. A. Hunt, M. W. Ammann, D. Weidner, L. Li, and L. Wang (2012a), The relative strength of perovskite and post-perovskite $NaCoF_3$, *Mineralogical Magazine*, *76*(4), 925 – 932, doi:10.1180/minmag.2012.076.4.09.

Dobson, D. P., R. McCormack, S. A. Hunt, M. W. Ammann, D. Weidner, L. Li, and L. Wang (2012b), The relative strength of perovskite and post-perovskite NaCoF3, *Mineralogical Magazine*, *76*(4), 925–932, doi:10.1180/minmag.2012.076.4.09.

Doornbos, D. J. (1974), The anelasticity of the inner core, *Geophysical Journal International*, *38*(2), 397–415, doi: 10.1111/j.1365-246x.1974.tb04131.x.

Durham, W. B., D. J. Weidner, S. I. Karato, and Y. B. Wang (2002), New developments in deformation experiments at high pressure, in *Plastic Deformation of Minerals and Rocks*, *Reviews in Mineralogy & Geochemistry*, vol. 51, edited by S. Karato and H. Wenk, pp. 21–49, Mineral. Soc. Am., doi:10.2138/gsrmg.51.1.21.

Dziewonski, A. M., and D. L. Anderson (1981), Preliminary reference Earth model, *Physics of the Earth and Planetary Interiors*, *25*(4), 297–356, doi:10.1016/0031-9201(81)90046-7.

Errandonea, D. (2010), The melting curve of ten metals up to 12 GPa and 1600 K, *Journal of Applied Physics*, *108*(3), 033,517, doi:10.1063/1.3468149.

Faul, U., and I. Jackson (2015), Transient creep and strain energy dissipation: An experimental perspective, *Annual Review of Earth and Planetary Sciences*, *43*(1), 541–569, doi:10.1146/annurev-{E}arth-060313-054732.

Fearn, D. R., D. E. Loper, and P. H. Roberts (1981), Structure of the Earth's inner core, *Nature*, *292*(5820), 232–233, doi:10.1038/292232a0.

Fei, Y. (1995), Thermal expansion, in *AGU Reference Shelf*, pp. 29–44, American Geophysical Union, doi:10.1029/rf002p0029.

Fei, Y., C. Murphy, Y. Shibazaki, A. Shahar, and H. Huang (2016), Thermal equation of state of hcp-iron: Constraint on the density deficit of Earth's solid inner core, *Geophysical Research Letters*, *43*(13), 6837–6843, doi: 10.1002/2016gl069456.

Fiquet, G. (2001), Sound velocities in iron to 110 Gigapascals, *Science*, *291*(5503), 468–471, doi:10.1126/science.291.5503.468.

Fischer, R. A., and A. J. Campbell (2015), The axial ratio of hcp Fe and Fe–Ni–Si alloys to the conditions of Earth's inner core, *American Mineralogist*, *100*, 2718–2724, doi:10.2138/am-2015-5191.

Frost, H., and M. Ashby (1982), *Deformation mechanism maps: the plasticity and creep of metals and ceramics*, Pergamon Press, Oxford, UK.

Gallier, J. H. (2000), *Curves and surfaces in geometric modeling: theory and algorithms*, Morgan Kaufmann series in computer graphics and geometric modeling, Morgan Kaufmann Publishers.

Gieske, J. H., and G. R. Barsch (1968), Pressure dependence of the elastic constants of single crystalline aluminum oxide, *Physica Status Solidi (b)*, *29*(1), 121–131, doi:10.1002/pssb.19680290113.

Gokhale, A., S. R, E.-W. Huang, S. Y. Lee, R. Prasad, S. S. Singh, and J. Jain (2019), Quantitative evaluation of grain boundary sliding and its dependence on orientation and temperature in pure zn, *Materials Letters*, *246*, 24 – 27, doi:https://doi.org/10.1016/j.matlet.2019.03.025.

Goto, T., O. L. Anderson, I. Ohno, and S. Yamamoto (1989), Elastic constants of corundum up to 1825 K, *Journal of Geophysical Research*, *94*(B6), 7588, doi:10.1029/jb094ib06p07588.

Gourdet, S., and F. Montheillet (2003), A model of continuous dynamic recrystallization, *Acta Materialia*, *51*(9), 2685 – 2699, doi:https://doi.org/10.1016/S1359-6454(03)00078-8.

Gribb, T. T., and R. F. Cooper (1998), Low-frequency shear attenuation in polycrystalline olivine: Grain boundary diffusion and the physical significance of the Andrade model for viscoelastic rheology, *Journal of Geophysical Research: Solid Earth*, *103*(B11), 27,267–27,279, doi:10.1029/98jb02786.

Harris, J. E., and B. C. Masters (1965), The stacking fault energy of zinc and magnesium, *physica status solidi (b)*, *9*(3), K181–K184, doi:https://doi.org/10.1002/pssb.19650090335.

Hernlund, J., K. Leinedweber, D. Locke, and J. A. Tyburzy (2006), A numerical model for steady-state temperature distributions in solid-medium high-pressure cell assemblies, *American Mineralogist*, *91*(2-3), 295–305, doi:10.2138/am.2006.1938.

Hielscher, R., C. B. Silbermann, E. Schmidl, and J. Ihlemann (2019), Denoising of crystal orientation maps, *Journal of Applied Crystallography*, *52*(5), 984–996, doi:10.1107/S1600576719009075.

Hunt, S. A., D. P. Dobson, L. Li, D. J. Weidner, and J. P. Brodholt (2010), Relative strength of the pyrope–majorite solid solution and the flow-law of majorite containing garnets, *Physics of the Earth and Planetary Interiors*, *179*(1-2), 87–95, doi:10.1016/j.pepi.2009.12.001.

Hunt, S. A., A. M. Walker, R. McCormack, D. P. Dobson, A. S. Wills, and L. Li (2011), The effect of pressure on thermal diffusivity in pyroxenes, *Mineralogical Magazine*, *75*(5), 2597–2610, doi:10.1180/minmag.2011.075.5.2597.

Hunt, S. A., D. R. Davies, A. M. Walker, R. J. McCormack, A. S. Wills, D. P. Dobson, and L. Li (2012), On the increase in thermal diffusivity caused by the perovskite to post-perovskite phase transition and its implications for mantle dynamics, *Earth and Planetary Science Letters*, *319 - 320*, 96 – 103, doi:10.1016/j.epsl.2011.12.009.

Hunt, S. A., D. J. Weidner, R. J. McCormack, M. L. Whitaker, E. Bailey, L. Li, M. T. Vaughan, and D. P. Dobson (2014), Deformation T-Cup: A new multi-anvil apparatus for controlled strain-rate deformation experiments at pressures above 18 GPa, *Review of Scientific Instruments*, *85*(8), 085,103, doi:10.1063/1.4891338.

Hunt, S. A., M. L. Whitaker, E. Bailey, E. Mariani, C. V. Stan, and D. P. Dobson (2019), An Experimental Investigation of the Relative Strength of the Silica Polymorphs Quartz, Coesite, and Stishovite, *Geochemistry, Geophysics, Geosystems*, *20*(4), 1975–1989, doi:10.1029/2018GC007842.

Irving, J. C., and A. Deuss (2011), Stratified anisotropic structure at the top of Earth's inner core: A normal mode study, *Physics of the Earth and Planetary Interiors*, *186*(1-2), 59–69, doi:10.1016/j.pepi.2011.03.003.

Jackson, I. (2015), Properties of rocks and minerals: Physical origins of anelasticity and attenuation in rock, in *Treatise on Geophysics*, pp. 539–571, Elsevier, doi:10.1016/b978-0-444-53802-4.00045-2.

Jackson, I., J. D. F. Gerald, and H. Kokkonen (2000), High-temperature viscoelastic relaxation in iron and its implications for the shear modulus and attenuation of the Earth's inner core, *Journal of Geophysical Research: Solid Earth*, *105*(B10), 23,605–23,634, doi:10.1029/2000jb900131.

Kanitpanyacharoen, W., S. Merkel, L. Miyagi, P. Kaercher, C. Tomé, Y. Wang, and H.-R. Wenk (2012), Significance of mechanical twinning in hexagonal metals at high pressure, *Acta Materialia*, *60*(1), 430 – 442, doi:https://doi.org/10.1016/j.actamat.2011.07.055.

Kennett, B. L. N., E. R. Engdahl, and R. Buland (1995), Constraints on seismic velocities in the Earth from traveltimes, *Geophysical Journal International*, *122*(1), 108–124, doi:https://doi.org/10.1111/j.1365-246X.1995.tb03540.x.

Ledbetter, H. M. (1977), Elastic properties of zinc: A compilation and a review, *Journal of Physical and Chemical Reference Data*, *6*(4), 1181–1203, doi:10.1063/1.555564.

Lee, L. C., and S. J. Morris (2010), Anelasticity and grain boundary sliding, *Proceedings of the Royal Society A: Mathematical, Physical and Engineering Sciences*, *466*(2121), 2651–2671, doi:10.1098/rspa.2009.0624.

Li, D., and R. H. Wagoner (2021), The nature of yielding and anelasticity in metals, *Acta Materialia*, *206*, 116,625, doi:https://doi.org/10.1016/j.actamat.2021.116625.

Li, L., and D. J. Weidner (2007), Energy dissipation of materials at high pressure and high temperature, *Review of Scientific Instruments*, *78*(5), 053,902, doi:10.1063/1.2735587.

Li, L., and D. J. Weidner (2008), Effect of phase transitions on compressional-wave velocities in the Earth's mantle, *Nature*, *454*(7207), 984–986, doi:10.1038/nature07230.

Li, L., P. Raterron, D. J. Weidner, and J. Chen (2003), Olivine flow mechanisms at 8 GPa, *Physics of The Earth and Planetary Interiors*, *138*, 113 – 129, doi:10.1016/S0031-9201(03)00065-7.

Li, X., and V. F. Cormier (2002), Frequency-dependent seismic attenuation in the inner core, 1. a viscoelastic interpretation, *Journal of Geophysical Research: Solid Earth*, *107*(B12), ESE 13–1–ESE 13–20, doi: 10.1029/2002jb001795.

Li, Y., L. Vočadlo, and J. P. Brodholt (2018), The elastic properties of hcp-Fe alloys under the conditions of the Earth's inner core, *Earth and Planetary Science Letters*, *493*, 118–127, doi:10.1016/j.epsl.2018.04.013.

Liebermann, R. C., and Y. Wang (1992), Characterization of sample environment in a uniaxial split-sphere apparatus, in *High-Pressure Research: Application to Earth and Planetary Sciences*, edited by Y. Syono and M. H. Manghnani, pp. 19–31, American Geophysical Union, doi:10.1029/gm067p0019.

Liu, S., D. Kent, H. Zhan, N. Doan, M. Dargusch, and G. Wang (2020), Dynamic recrystallization of pure zinc during high strain-rate compression at ambient temperature, *Materials Science and Engineering: A*, *784*, 139,325, doi:https://doi.org/10.1016/j.msea.2020.139325.

Lloyd, G. E. (1987), Atomic number and crystallographic contrast images with the SEM: a review of backscattered electron techniques, *Mineralogical Magazine*, *51*, 3–19, doi:10.1180/minmag.1987.051.359.02.

Lythgoe, K., A. Deuss, J. Rudge, and J. Neufeld (2014), Earth's inner core: Innermost inner core or hemispherical variations?, *Earth and Planetary Science Letters*, *385*, 181–189, doi:10.1016/j.epsl.2013.10.049.

Mäkinen, A. M., A. Deuss, and S. A. T. Redfern (2014), Anisotropy of Earth's inner core intrinsic attenuation from seismic normal mode models, *Earth and Planetary Science Letters*, *404*, 354–364, doi:10.1016/j.epsl.2014.08.009.

Mao, Z., J.-F. Lin, J. Liu, A. Alatas, L. Gao, J. Zhao, and H.-K. Mao (2012), Sound velocities of Fe and Fe-Si alloy in the Earth's core, *Proceedings of the National Academy of Sciences*, *109*(26), 10,239–10,244, doi:10.1073/pnas.1207086109.

Marquardt, H., J. Buchen, A. S. J. Mendez, A. Kurnosov, M. Wendt, A. Rothkirch, D. Pennicard, and H. Liermann (2018), Elastic Softening of (Mg 0.8 Fe 0.2)O Ferropericlase Across the Iron Spin Crossover Measured at Seismic Frequencies, *Geophysical Research Letters*, *45*(14), 6862–6868, doi:10.1029/2018GL077982.

Matsunaga, T., T. Kameyama, S. Ueda, and E. Sato (2010), Grain boundary sliding during ambient-temperature creep in hexagonal close-packed metals, *Philosophical Magazine*, *90*(30), 4041–4054, doi:10.1080/14786435.2010.502883.

Means, W. D. (1981), The concept of steady-state foliation, *Tectonophysics*, *78*(1), 179 – 199, doi:10.1016/0040-1951(81)90013-5.

Merkel, S., H.-R. Wenk, P. Gillet, H. kwang Mao, and R. J. Hemley (2004), Deformation of polycrystalline iron up to 30 GPa and 1000 K, *Physics of the Earth and Planetary Interiors*, *145*(1-4), 239–251, doi:10.1016/j.pepi.2004.

04.001.

Miyagi, L., M. Kunz, J. Knight, J. Nasiatka, M. Voltolini, and H.-R. Wenk (2008), In situ phase transformation and deformation of iron at high pressure and temperature, *Journal of Applied Physics*, *104*(10), 103,510, doi:10.1063/1.3008035.

Montheillet, F., and J. J. Jonas (2003), *Recrystallization, Dynamic*, American Cancer Society, doi:https://doi.org/10.1002/3527600434.eap388.

Morelli, A., A. M. Dziewonski, and J. H. Woodhouse (1986), Anisotropy of the inner core inferred from PKIKP travel times, *Geophysical Research Letters*, *13*(13), 1545–1548, doi:10.1029/gl013i013p01545.

Moser, Z. (1991), The Pt-Zn (platinum-zinc) system, *Journal of Phase Equilibria*, *12*, 439–443, doi:10.1007/BF02645964.

Murthy, G. S., and D. H. Sastry (1982), Impression creep of zinc and the rate-controlling dislocation mechanism of plastic flow at high temperatures, *physica status solidi (a)*, *70*(1), 63–71, doi:10.1002/pssa.2210700110.

Niessen, P., E. L. Holmes, and W. C. Winegard (1963), Grain Growth in Zone-Refined Zinc, *Canadian Metallurgical Quarterly*, *2*(2), 177–185, doi:10.1179/cmq.1963.2.2.177.

Niu, F., and L. Wen (2001), Hemispherical variations in seismic velocity at the top of the Earth's inner core, *Nature*, *410*(6832), 1081–1084, doi:10.1038/35074073.

Nowick, A. S., and B. S. Berry (1972), *Anelastic Relaxation in Crystalline Solids*, Academic Press.

Nuss, J., U. Wedig, A. Kirfel, and M. Jansen (2010), The structural anomaly of zinc: Evolution of lattice constants and parameters of thermal motion in the temperature range of 40 to 500 K, *Zeitschrift für anorganische und allgemeine Chemie*, *636*(2), 309–313, doi:10.1002/zaac.200900460.

Pejić, T., R. Hawkins, M. Sambridge, and H. Tkalčić (2019), Transdimensional bayesian attenuation tomography of the upper inner core, *Journal of Geophysical Research: Solid Earth*, *124*(2), 1929–1943, doi:10.1029/2018jb016400.

Poirier, J., and G. Price (1999), Primary slip system of ϵ-iron and anisotropy of the earth's inner core, *Physics of the Earth and Planetary Interiors*, *110*(3), 147–156, doi:https://doi.org/10.1016/S0031-9201(98)00131-9.

Pratt, W. K. (1991), *Digital Image Processing*, pp. 171–186, Wiley.

Prescher, C., L. Dubrovinsky, E. Bykova, I. Kupenko, K. Glazyrin, A. Kantor, C. McCammon, M. Mookherjee, Y. Nakajima, N. Miyajima, R. Sinmyo, V. Cerantola, N. Dubrovinskaia, V. Prakapenka, R. Rüffer, A. Chumakov, and M. Hanfland (2015), High poisson's ratio of Earth's inner core explained by carbon alloying, *Nature Geoscience*, *8*(3), 220–223, doi:10.1038/ngeo2370.

Price, P. B. (1961), Nucleation and growth of twins in dislocation-free zinc crystals, *Proceedings of the Royal Society of London. Series A. Mathematical and Physical Sciences*, *260*(1301), 251–262, doi:10.1098/rspa.1961.0031.

Roberts, J. M., and N. Brown (1962), Low ferquency internal friction in zinc single crystals, *Acta Metalurgica*, *10*, 430 – 441.

Romanowicz, B., and B. Mitchell (2015), Deep Earth structure: Q of the Earth from crust to core, in *Treatise on Geophysics*, pp. 789–827, Elsevier, doi:10.1016/b978-0-444-53802-4.00021-x.

Sakamaki, T., E. Ohtani, H. Fukui, S. Kamada, S. Takahashi, T. Sakairi, A. Takahata, T. Sakai, S. Tsutsui, D. Ishikawa, R. Shiraishi, Y. Seto, T. Tsuchiya, and A. Q. R. Baron (2016), Constraints on Earth's inner core composition inferred from measurements of the sound velocity of hcp-iron in extreme conditions, *Science Advances*, *2*(2), e1500,802, doi:10.1126/sciadv.1500802.

Shearer, P. M. (1994), Constraints on inner core anisotropy from PKP(DF) travel times, *Journal of Geophysical Research: Solid Earth*, *99*(B10), 19,647–19,659, doi:10.1029/94jb01470.

Shirn, G., E. Wajda, and H. Huntington (1953), Self-diffusion in zinc, *Acta Metallurgica*, *1*(5), 513 – 518, doi:https://doi.org/10.1016/0001-6160(53)90081-9.

Singh, S. C. (2000), On the presence of liquid in Earth's inner core, *Science*, *287*(5462), 2471–2474, doi:10.1126/science.287.5462.2471.

Srinivasan, R., and R. R. Rao (1971), Anharmonic properties of the hexagonal metals, magnesium, zinc and beryllium – i. lattice dynamics and third order elastic constants, *Journal of Physics and Chemistry of Solids*, *32*(8), 1769–1788, doi:10.1016/s0022-3697(71)80143-9.

Stein, S., and M. Wysession (2013), *An Introduction to Seismology, Earthquakes, and Earth Structure*, John Wiley & Sons.

Suda, N., and Y. Fukao (1990), Structure of the inner core inferred from observations of seismic core modes, *Geophysical Journal International*, *103*(2), 403–413, doi:10.1111/j.1365-246x.1990.tb01779.x.

Sumita, I., and M. Bergman (2015), Inner core dynamics, in *Treatise on Geophysics*, pp. 297–316, Elsevier, doi:10.1016/b978-0-444-53802-4.00143-3.

Sundberg, M., and R. F. Cooper (2010), A composite viscoelastic model for incorporating grain boundary sliding and transient diffusion creep: correlating creep and attenuation responses for materials with a fine grain size, *Philosophical Magazine*, *90*(20), 2817–2840, doi:10.1080/14786431003746656.

Tagawa, S., K. Ohta, K. Hirose, C. Kato, and Y. Ohishi (2016), Compression of Fe-Si-H alloys to core pressures, *Geophysical Research Letters*, *43*(8), 3686–3692, doi:10.1002/2016gl068848.

Takahashi, S. (1952), Anelasticity of zinc, *Journal of Applied Physics*, *23*(8), 866–868, doi:10.1063/1.1702321.

Tateno, S., K. Hirose, Y. Ohishi, and Y. Tatsumi (2010), The structure of iron in Earth's inner core, *Science*, *330*(6002), 359–361, doi:10.1126/science.1194662.

Tateno, S., K. Hirose, T. Komabayashi, H. Ozawa, and Y. Ohishi (2012), The structure of Fe-Ni alloy in Earth's inner core, *Geophysical Research Letters*, *39*(12), L052,103, doi:10.1029/2012GL052103.

Tateno, S., Y. Kuwayama, K. Hirose, and Y. Ohishi (2015), The structure of Fe–Si alloy in Earth's inner core, *Earth and Planetary Science Letters*, *418*, 11–19, doi:10.1016/j.epsl.2015.02.008.

Tegart, W. J. M., and O. D. Sherby (1958), Activation energies for high temperature creep of polycrstalline zinc, *Philosophical Magazine*, *3*(35), 1287–1296, doi:10.1080/14786435808233311.

Thomas, S., K. M. Ajith, and M. C. Valsakumar (2017), Empirical potential influence and effect of temperature on the mechanical properties of pristine and defective hexagonal boron nitride, *Materials Research Express*, *4*(6), 065,005, doi:10.1088/2053-1591/aa72bf.

Thompson, D. O. (1955), Temperature dependent creep in zinc crystals, *Journal of Applied Physics*, *26*, 280–285, doi:10.1063/1.1721978.

Trucco, E., and A. Verri (1998), *Introductory Techniques for 3-D Computer Vision*, Prentice-Hall, Upper Saddle River, NJ, 343 pp.

Tutcuoglu, A., A. Vidyasagar, K. Bhattacharya, and D. Kochmann (2019), Stochastic modeling of discontinuous dynamic recrystallization at finite strains in hcp metals, *Journal of the Mechanics and Physics of Solids*, *122*, 590 – 612, doi:https://doi.org/10.1016/j.jmps.2018.09.032.

Vočadlo, L., D. P. Dobson, and I. G. Wood (2009), Ab initio calculations of the elasticity of hcp-Fe as a function of temperature at inner-core pressure, *Earth and Planetary Science Letters*, *288*(3-4), 534–538, doi:10.1016/j.epsl.2009.10.015.

Wajda, E. S. (1954), Grain boundary self-diffusion in zinc, *Acta Metallurgica*, *2*(2), 184 – 187, doi:https://doi.org/10.1016/0001-6160(54)90157-1.

Walker, A. M., and J. Wookey (2012), MSAT – a new toolkit for the analysis of elastic and seismic anisotropy, *Computers & Geosciences*, *49*, 81–90, doi:10.1016/j.cageo.2012.05.031.

Walker, D., M. A. Carpenter, and C. M. Hitch (1990), Some simplifications to multianvil devices for high pressure experiments, *American Mineralogist*, *75*(9-10), 1020–1028.

Wang, Y., and J. Huang (2003), Texture analysis in hexagonal materials, *Materials Chemistry and Physics*, *81*(1), 11–26, doi:https://doi.org/10.1016/S0254-0584(03)00168-8.

Wang, Y., B. Durham, I. C. Getting, and D. J. Weidner (2003), The deformation-DIA: A new apparatus for high temperature triaxial deformation to pressures up to 15 GPa, *Review of Scientific Instruments*, *74*(6), 3002 – 3011, doi:10.1063/1.1570948.

Watanabe, T., S.-I. Kimura, and S. Karashima (1984), The effect of a grain boundary structural transformation on sliding in <1010>-tilt zinc bicrystals, *Philosophical Magazine A*, *49*(6), 845–864, doi:10.1080/01418618408236566.

Weidner, D. J., M. T. Vaughan, L. Wang, H. Long, L. Li, N. A. Dixon, and W. B. Durham (2010), Precise stress measurements with white synchrotron X-rays, *Review of Scientific Instruments*, *81*, 013,903, doi:10.1063/1.

3263760.

Wheeler, J., D. Prior, Z. Jiang, R. Spiess, and P. Trimby (2001), The petrological significance of misorientations between grains, *Contributions to Mineralogy and Petrology*, *141*(1), 109–124, doi:10.1007/s004100000225.

Wheeler, J., E. Mariani, S. Piazolo, D. Prior, P. Trimby, and M. Drury (2009), The weighted Burgers vector: a new quantity for constraining dislocation densities and types using electron backscatter diffraction on 2D sections through crystalline materials, *Journal of Microscopy*, *233*(3), 482–494, doi:10.1111/j.1365-2818.2009.03136.x.

Woodhouse, J. H., D. Giardini, and X.-D. Li (1986), Evidence for inner core anisotropy from free oscillations, *Geophysical Research Letters*, *13*(13), 1549–1552, doi:10.1029/gl013i013p01549.

Wuttig, M., A. Aning, and T. Suzuki (1981), Autooscillations in zinc, *Scripta Metallurgica*, *15*, 1237–1239, doi:10.1016/0036-9748(81)90306-9.

Yoo, M., S. Agnew, J. Morris, and K. Ho (2001), Non-basal slip systems in HCP metals and alloys: source mechanisms, *Materials Science and Engineering: A*, *319-321*, 87–92, doi:10.1016/s0921-5093(01)01027-9.

Yoo, M. H., and C. T. Wei (1967), Slip modes of hexagonal-close-packed metals, *Journal of Applied Physics*, *38*(11), 4317–4322, doi:10.1063/1.1709121.

Yu, W.-c., and L. Wen (2006), Inner core attenuation anisotropy, *Earth and Planetary Science Letters*, *245*(3-4), 581–594, doi:10.1016/j.epsl.2006.03.043.

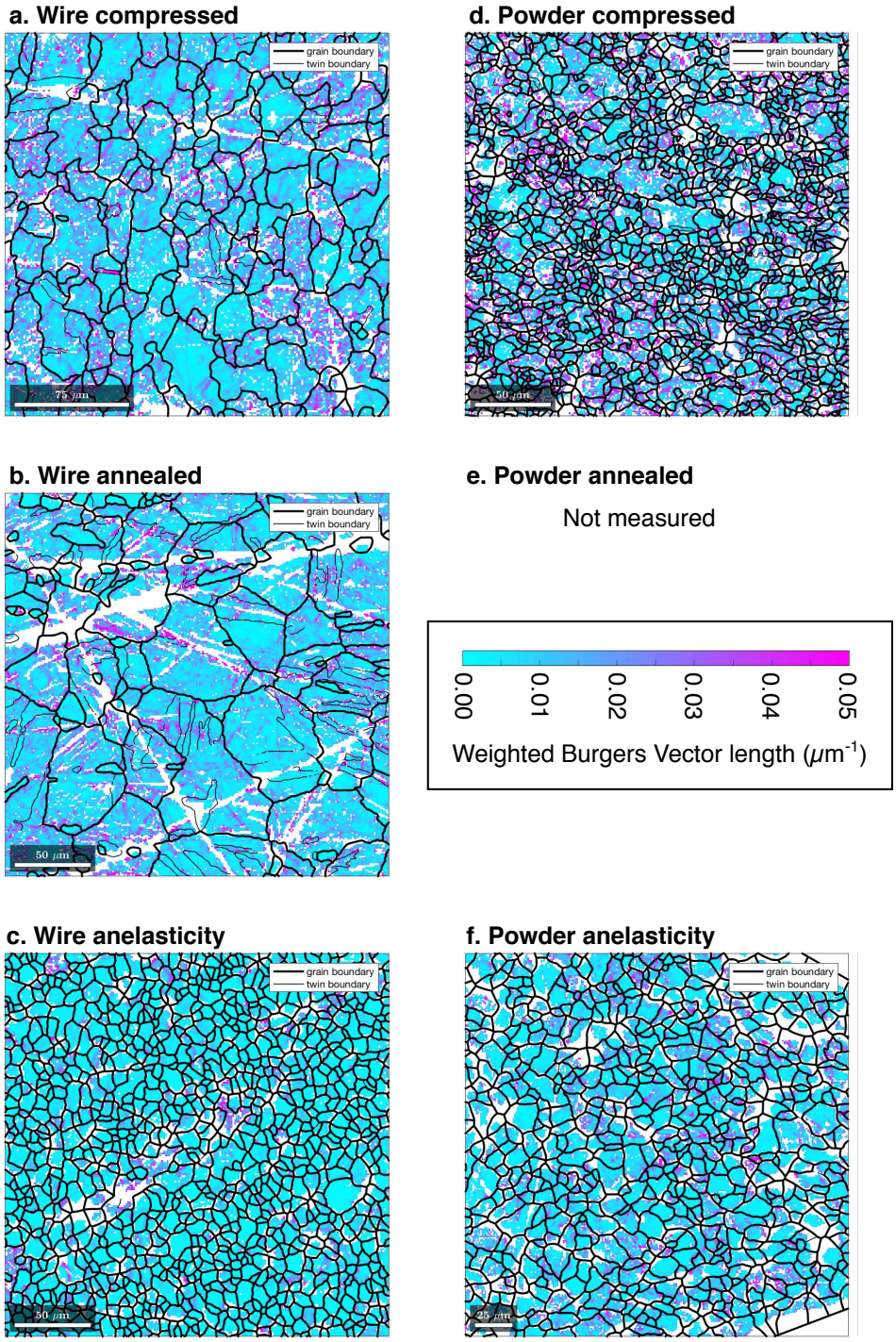

Figure S1. Weighted Burgers Vectors Length maps for EBSD data. The samples, layout and areas plotted are the same as those in Figure 5. All maps are to the same colour scale. White areas in the EBSD maps are where the sample was not indexed or data discarded; the linear white features in a and b are scratches from which data has been discarded. The cumulative WBV length distribution for each map is plotted in Figures 6e and 6f.